Selfregulated Star Formation in Galactic Disks, Influenced by the Accretion of Cosmic Gas

Maximilian Brunner

SIGILL·UNIVERSITAT·LUDOVIC·MAXIM·

Munich 2012

Selfregulated Star Formation in Galactic Disks, Influenced by the Accretion of Cosmic Gas

Master-Thesis

at the
Ludwig–Maximilians–University Munich

handed in by

Maximilian Brunner
(Matr. Nr.: 4037020)
born 29.07.1987 in Kolbermoor

Supervisors
Prof. Dr. Andreas Burkert

and
Christian Alig

Munich, December 4, 2012

Evaluator: Prof. Dr. Andreas Burkert

Contents

List of Figures

Introduction

The mechanisms of star formation, its causes, and its consequences are tremendously important for the evolution of galaxies, leading to great interest in continuous research on the topic from many different fields in astrophysics. Observations indicate that most of the star formation takes place in clouds of molecular hydrogen that collapse and fragment under their own gravity (Espada et al. [2012], Brand et al. [2012]). Therefore, to understand star formation one must further investigate the physics that lead to the formation of these molecular clouds, and by extension the formation and evolution of galaxies and galactic disks. Although the rapid improvement in observational instruments over the last decades now allows us to look at galaxies, both the Milky Way and the local group in which it resides (Kennicutt and Evans [2012]), as well as those situated in clusters or isolated up to high redshifts(Oliver et al. [2012]), the fact that these processes take place on timescales far longer than a human lifetime means that observations alone have a hard time of explaining and describing all the physics involved. As such, numerical simulations play an ever increasing role in research, facilitated by ongoing technological progress.

When it comes to simulations concerning star formation, there exists a plethora of different approaches, which are divided by numerical methods used but also by the scales on which the calculations take place. Simulations of individual molecular clouds grant great insight into fragmentation and collapse mechanisms, crucial for understanding the way stars form(Glover and Mac Low [2007], Glover and Clark [2012], Clark et al. [2012]). However, they can not, by definition, answer the questions about the large scale processes affecting whole galaxies. This is aggravated by the fact that, although star formation takes place on a scale smaller than the size of a typical galaxy, empirical discoveries like the Kennicutt-Schmidt law of star formation (Kennicutt [1998]) and the Tully-Fisher relation (Tully and Fisher [1977]) imply that there is a coupling between the formation of individual stars and the greater behaviour of the galaxy that itself influences further star formation. Furthermore, theoretical models predict that the accretion of hydrogen into the galaxy should also significantly impact both the internal structure of the galaxy and subsequently the formation of stars therein (Dekel et al. [2009], Bouché et al. [2010]). Thus it can not be enough to simply understand the microphysics involved in star formation, but one also has to take into account the larger scales of whole galaxies.

Cosmological simulations on the other hand that calculate vast areas on the order of megaparsecs over large timescales up to the age of the universe(Heß and Springel [2012], Biffi et al. [2012]), are ideally suited for further investigating the formation of structure and therefore galaxies but so far lack the accuracy to actually resolve individual galaxies to a degree that allows conclusions as to the physical processes governing the actual formation of stars. While these simulations are able to give great insights into the interaction between galaxies and the way in which they form, evolve, and accrete more hydrogen from their surroundings, this lack of resolution means that, in order to calculate internal dynamics of galaxies(Springel and Hernquist [2003]), the involved codes often apply strong simplifications that only allow the most tentative speculations.

Another possible approach would be to simulate an isolated galaxy that is sufficiently resolved to guarantee correct treatment of the dynamics of the interstellar medium, as well as calculate star formation scenarios with only a minimum of assumptions that might bias the results(Dobbs [2011]). In this work, we carry out such a simulation with the goal of giving a self-consistent view that includes a full hydrodynamical, as well as gravitational treatment of hydrogen in a galactic disk inside a Dark Matter halo. This includes a star forming algorithm, complete with feedback from supernovae and draining of the hydrogen reservoir, as well as a rudimentary prescription of additional accretion onto the disk.

The thesis is organized in the following way. First we give a brief overview over the physics and observed phenomena involved in star formation on all scales. Second we describe the numerical implementation chosen for the simulations presented in the following chapter. Lastly we summarize our findings and draw a conclusion.

1 Theoretical & Observational Background

1.1 Galactic Density Distributions

Observations of Galaxies show that in most Galactic Disks, the luminosity I has an exponential distribution over radius R of the Form

$$I(R) = I_0 e^{-R/R_{\mathrm{d}}}, \tag{1.1}$$

where I_0 is the central luminosity and R_{d} is the scale radius (Freeman [1970]).

It is now a reasonable assumption that the luminosity is directly correlated to the surface density Σ , which then takes the form

$$\Sigma(R) = \Sigma_0 e^{-R/R_{\mathrm{d}}}, \tag{1.2}$$

with central surface density Σ_0. We would now like to calculate the gravitational potential Φ of such a disk, since this is generally more useful for calculating the dynamics of particles. This derivation closely follows (Binney and Tremaine [2008]). For this we treat the disk as a very flat spheroid. A homogeneous spheroid has surface density

$$\Sigma\left(a, R\right) = 2\rho q\sqrt{a^2 - R^2}, \tag{1.3}$$

where q is its axial ratio c/a , a and c are its semi-axes, ρ is its density, and R is the cylindrical radius. Differentiating equation 1.3 with respect to a gives us the surface density for a thin homoeiod

$$\delta\Sigma\left(a, R\right) = \frac{\Sigma_h \delta a}{\sqrt{a^2 - R^2}}, \tag{1.4}$$

where we substituted $\Sigma_h \equiv 2\rho q a$. We can now deconstruct any thin disk into a series of such homoeiods, whose combined surface density is the same as that of the disk. Mathematically speaking, we want to solve

$$\Sigma\left(R\right) = \int\limits_R^\infty \mathrm{d}a \frac{\Sigma_h\left(a\right)}{\sqrt{a^2 - R^2}} \tag{1.5}$$

for $\Sigma_h\left(a\right)$. This yields

$$\Sigma_h\left(a\right) = -\frac{2}{\pi}\frac{\mathrm{d}}{\mathrm{d}a}\int\limits_a^\infty \frac{R\Sigma\left(R\right)}{\sqrt{R^2 - a^2}}. \tag{1.6}$$

Additionally, the potential of a thin homoeiod is

$$\delta\Phi = -2\pi G\Sigma_h \delta a \arcsin\left(\frac{2a}{\sqrt{z^2 + \left(a + R\right)^2} + \sqrt{z^2 + \left(a - R\right)^2}}\right), \tag{1.7}$$

where G is the gravitational constant. Inserting equation 1.6 into equation 1.7 and integrating them gives us the potential of a thin disk as

$$\Phi(R,z) = -2\sqrt{2}G \int_0^\infty \mathrm{d}a \frac{[(a+R)/\sqrt{+}] - [(a-R)/\sqrt{-}]}{\sqrt{R^2 - z^2 - a^2 + \sqrt{+}\sqrt{-}}} \times \int_a^\infty \mathrm{d}R' \frac{R'\Sigma(R')}{\sqrt{R'^2 - a^2}}, \quad (1.8)$$

with

$$\sqrt{\pm} = \sqrt{z^2 + (a \pm R)^2}. \quad (1.9)$$

The second integration in equation 1.8 yields

$$\int_a^\infty \mathrm{d}R' \frac{R'\Sigma(R')}{\sqrt{R'^2 - a^2}} = \Sigma_0 a K_1(a/R_\mathrm{d}), \quad (1.10)$$

where K_1 denotes the modified Bessel function. This can now be used to calculate the mid plane potential of the disk, which turns out to be

$$\Phi(R,0) = -\pi G \Sigma_0 R[I_0(y)K_1(y) - I_1(y)K_0(y)], \quad (1.11)$$

with

$$y \equiv \frac{R}{2R_\mathrm{d}} \quad (1.12)$$

and the modified Bessel functions K_0, K_1, I_0 and I_1.

Knowing the potential we can now determine the rotational velocity v_c to be

$$\boxed{v_\mathrm{c}^2 = R\frac{\partial \Phi}{\partial R} = 4\pi G \Sigma_0 R_\mathrm{d} y^2 [I_0(y)K_0(y) - I_1(y)K_1(y)]}. \quad (1.13)$$

Technically, this equation is only for the limit of an infinitesimally thin disk, which can be shown to still remain valid for disks with scale height small compared to their scale readius.

Of course, we also want to discuss the vertical structure of a galactic disk. We begin with the Poisson equation under the assumption that only matter in the equatorial plane in the disk is relevant for gravity and therefore we only need the dependence on the distance z to the equatorial plane:

$$\frac{d^2\Phi}{dz^2} = 4\pi G\rho \quad (1.14)$$

with density ρ . Next, we assume that the disk is in thermal equilibrium, which reduces the Euler equation to

$$\frac{dp}{dz} = -\rho\frac{d\Phi}{dz}, \quad (1.15)$$

where p denotes pressure. To express the pressure in terms of density, we assume that the disk is made up of isothermal sheets and get the equation of state as

$$p = c_s^2\rho, \quad (1.16)$$

where c_s is the sound speed. By substituting equation 1.16 into equation 1.15, dividing by ρ, differentiating by z, and using equation 1.14 to eliminate $\frac{d^2\Phi}{dz^2}$ we get

$$\frac{d}{dz}\left(\frac{1}{\rho}\frac{d\rho}{dz}\right) = -\frac{4\pi G}{c_s^2}\rho. \tag{1.17}$$

By substituting variables in a favourable way and some calculations (see (Spitzer [1942]) for a more detailed discussion) this equation can be solved and gives

$$\rho\left(z\right) = \rho_0 \mathrm{sech}^2\left(\frac{z}{2z_0}\right), \tag{1.18}$$

with ρ_0 being the mid plane density, and scale height

$$z_0 = \frac{c_s}{\sqrt{8\pi G\rho_0}}. \tag{1.19}$$

Figure 1.1 illustrates the behaviour of $\rho(z)$, namely that it can be approximated by

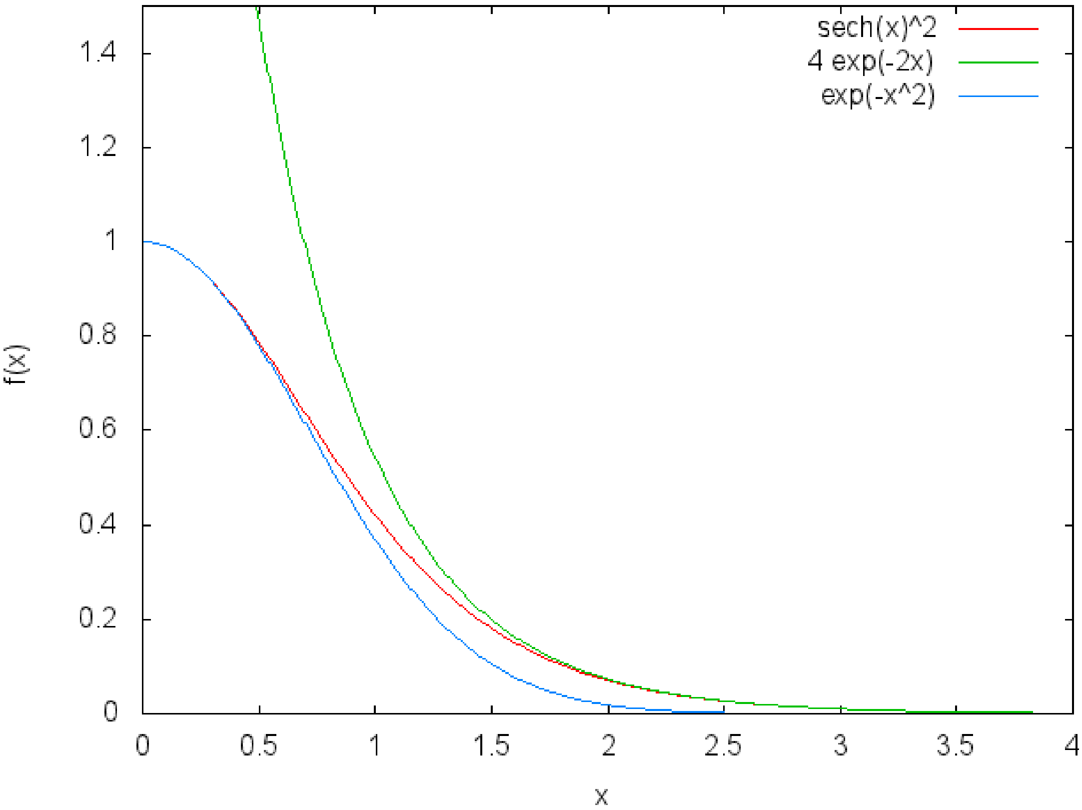

Fig. 1.1: Illustration of how the function $\mathrm{sech}^2(x)$(red) from equation 1.19 can be approximated by $4e^{-2x}$(green) for small radii, and e^{-x^2}(blue) for large radii respectively.

a Gaussian for small x and by an exponential function for large x. Using the fact that ρ_0 is nothing else but the surface density, we get

$$\boxed{\rho\left(R,z\right)=\Sigma_0 e^{-\frac{R}{R_\mathrm{d}}}\operatorname{sech}^2\left(\frac{z}{z_0}\right)}. \tag{1.20}$$

It is generally assumed that all Galaxies reside in larger Dark Matter halos, whose gravitation also has a tremendous impact on the baryonic matter within. To further study its density distribution, we start with the rotatinal velocity

$$v_{\mathrm{c,dm}}^2\left(r\right)=r\frac{d\Phi}{dr}. \tag{1.21}$$

By taking the halo as being spherically symmetric, this simplifies to

$$v_{\mathrm{c,dm}}^2\left(r\right)=\frac{GM\left(r\right)}{r} \tag{1.22}$$

with $M\left(r\right)$ being the mass inside a sphere of radius r. For a rotation curve we use

$$v_{\mathrm{c,dm}}^2\left(r\right)=v_0^2\frac{r^2}{\left(r+\epsilon\right)^2}, \tag{1.23}$$

with the core radius ϵ. This is the simplest parametrisation that gives us a rotation curve that is linear in r in the centre and becomes flat with an asymptotic limit of v_0 for large radii. This now allows us to solve for

$$M\left(r\right)=\frac{v_0^2}{G}\frac{r^3}{\left(r+\epsilon\right)^2}. \tag{1.24}$$

Next we consider the fact that the mass inside a sphere can also be calculated by

$$M\left(r\right)=\int\limits_V\rho_{dm}\left(\vec{r}\right)d\vec{r}=\int\limits_0^r 4\pi\rho_{dm}\left(r'\right)r'^2dr', \tag{1.25}$$

written in spherical coordinates under the assumption of spherical symmetry of the halo. Using the fundamental theorem of calculus, we can now write

$$\frac{dM\left(r\right)}{dr}=4\pi\rho_{dm}\left(r\right)r^2, \tag{1.26}$$

which can easily be solved for

$$\rho_{dm}\left(r\right)=\frac{1}{4\pi r^2}\frac{dM\left(r\right)}{dr}. \tag{1.27}$$

Differentiating equation 1.24 and then substituting into equation 1.27 then gives us the density distribution of the Dark Matter

$$\boxed{\rho_{dm}\left(r\right)=\frac{v_0^2}{4\pi G}\left(\frac{3}{\left(r+\epsilon\right)^2}-\frac{2r}{\left(r+\epsilon\right)^3}\right)}. \tag{1.28}$$

1.2 Density Perturbations

So far we have always treated the matter in a Disk to be more or less homgeneously distributed. Most systems will inevitably show perturbations of some kind that can drastically alter the expected behaviour. In the following paragraphs we want to give a short overview of how perturbations that arise can be maintained in a razor thin disk of fluid-like particles. We again follow (Binney and Tremaine [2008]) very closely for the following derivation. We begin with the Euler equation in cylindrical coordinates:

$$\frac{\partial v_R}{\partial t} + v_R \frac{\partial v_R}{\partial R} + \frac{v_\phi}{R}\frac{\partial v_R}{\partial \phi} - \frac{v_\phi^2}{R} = -\frac{\partial \Phi}{\partial R} - \frac{1}{\Sigma_\mathrm{d}}\frac{\partial p}{\partial R} \tag{1.29}$$

$$\frac{\partial v_\phi}{\partial t} + v_R \frac{\partial v_\phi}{\partial R} + \frac{v_\phi}{R}\frac{\partial v_\phi}{\partial \phi} - \frac{v_\phi v_R}{R} = -\frac{\partial \Phi}{\partial \phi} - \frac{1}{\Sigma_\mathrm{d} R}\frac{\partial p}{\partial \phi}, \tag{1.30}$$

where Σ_d is the surface density of the disk. We now start with an unperturbed axisymmetric disk in a steady state, which will be denoted in the following with the subscript "0". The prerequisites necessary for such a disk, namely $v_{R0} = 0$ and $\partial\Phi_0/\partial\phi = \partial p_0/\partial\phi = 0$, then simplify the Euler equations to

$$\frac{v_{\phi 0}^2}{R} = \frac{\mathrm{d}\Phi_0}{\mathrm{d}R} + c_s^2 \frac{\mathrm{d}}{\mathrm{d}R}\ln\Sigma_0. \tag{1.31}$$

We also need an equation of state for the further treatment. In this case we take the rather simple equation

$$p = K\Sigma_\mathrm{d}^\gamma, \tag{1.32}$$

with K being a constant that depends on the specific entropy, and γ being the adiabatic index. From this equation we can trivially derive the sound speed to be

$$c_s^2\left(\Sigma_0\right) = \left(\frac{\mathrm{d}p}{\mathrm{d}\Sigma}\right)_{\Sigma_0} = \gamma K \Sigma_0^{\gamma-1}. \tag{1.33}$$

We can further simplify the equations of motion by replacing the pressure with the specific enthalpy

$$h = \frac{\gamma}{\gamma - 1} K \Sigma_\mathrm{d}^{\gamma-1}. \tag{1.34}$$

We now introduce perturbations of the form $v_R = \varepsilon v_{R1}$, $v_\phi = v_{\phi 0} + \varepsilon v_{\phi 1}$, $h = h_0 + \varepsilon h_1$, $\Sigma_\mathrm{d} = \Sigma_0 + \varepsilon\Sigma_1$ and $\Phi = \Phi_0 + \varepsilon\Phi_1$, where ε is a very small number. Inserting that in the equation of motion and only evaluating terms that are linear in ε we get

$$\frac{\partial v_{R1}}{\partial t} + \Omega \frac{\partial v_{R1}}{\partial \phi} - 2\Omega v_{\phi 1} = -\frac{\partial}{\partial R}\left(\Phi_1 + h_1\right) \tag{1.35}$$

$$\frac{\partial v_{\phi 1}}{\partial t} + \left[\frac{\mathrm{d}\left(\Omega R\right)}{\mathrm{d}R} + \Omega\right] v_{R1} + \Omega \frac{\partial v_{\phi 1}}{\partial \phi} = -\frac{1}{R}\frac{\partial}{\partial \phi}\left(\Phi_1 + h_1\right), \tag{1.36}$$

where Ω is the circular frequency $v_{\phi 0}/R$. We can now make the Ansatz that the perturbations are of the form

$$v_{R1} = \mathrm{Re}\left[v_{Ra}\left(R\right)e^{\mathrm{i}(m\phi-\omega t)}\right], \tag{1.37}$$

with m-fold rotational symmetry, and angular frequency ω.

We also need the equation of continuity to link the velocities to the surface density. For terms linear in ε and in cylindrical coordinates, this equation is of the form

$$\frac{\partial \Sigma_{\mathrm{d1}}}{\partial t} + \Omega\frac{\partial \Sigma_{\mathrm{d1}}}{\partial \phi} + \frac{1}{R}\frac{\partial}{\partial R}\left(R v_{Ra}\Sigma_0\right) + \frac{\Sigma_0}{R}\frac{\partial v_{\phi 1}}{\partial \phi} = 0, \tag{1.38}$$

which we can calculate to be

$$-\,\mathrm{i}\left(\omega - m\Omega\right)\Sigma_{\mathrm{da}} + \frac{1}{R}\frac{\mathrm{d}}{\mathrm{d}R}\left(R v_{Ra}\Sigma_0\right) + \frac{\mathrm{i}m\Sigma_0}{R}v_{\phi a} = 0. \tag{1.39}$$

If we now assume that a tight-winding, short-wavelength approximation is viable, meaning that the radial wavelength of the debsity perturbations is much smaller than the disk radius, a reasonable assumption for most obeerved disks, we can write the gravitational potential imposed by these density waves as

$$\Phi_a(R) = F(R)e^{i\int^{R} k\mathrm{d}R}, \tag{1.40}$$

where F is the amplitutde of the perturbation and k is its radial wavenumber. Linking the potential to the surface density via Poisson's equation and omitting terms of the order $|kR| \gg 1$ we arrive at the velocities being

$$v_{Ra} = -\frac{\left(\omega - m\Omega\right)}{\Delta}k\left(\Phi_a + h_a\right) \tag{1.41}$$

$$v_{\phi a} = -\frac{2\mathrm{i}B}{\Delta}k\left(\Phi_a + h_a\right). \tag{1.42}$$

Similarly, the continuity equation now has the form

$$-\left(\omega - m\Omega\right)\Sigma_{\mathrm{da}} + k\Sigma_0 v_{Ra} = 0. \tag{1.43}$$

Combining these equations and assuming self-consistency we get the dispersion relation

$$\left(\omega - m\Omega\right)^2 = \kappa^2 - 2\pi G\Sigma_0|k| + c_s^2k^2, \tag{1.44}$$

where κ is the epicyclic frequency

$$\kappa^2 = R\frac{\mathrm{d}\Omega^2}{\mathrm{d}R} + 4\Omega^2. \tag{1.45}$$

For an axisymmetric perturbation, the disk becomes unstable if the right side is negative and therefore the limit of stability is defined as

$$\kappa^2 - 2\pi G\Sigma_0|k| + c_s^2k^2 = 0. \tag{1.46}$$

This equation is not allowed to have a solution for any positve $|k|$, since the equation is quadratic, the stability criterion can easily be derived to be

$$\boxed{Q \equiv \frac{c_s \kappa}{\pi G \Sigma_0} > 1}. \tag{1.47}$$

This can be understood as a condition for local stability (Toomre [1964]). If Q is smaller than unity, perturbation waves of a wavelength smaller than the critical wavelength can grow while travelling through the unstable region.

1.3 Interstellar Medium

Knowing that a fluid disk can be in a state of instability, the next question to be asked is how such a disk can arrive at this state. For that we have to take into account the different constituents of the Interstellar Medium and their interactions with each other and radiation from different sources. Observations show that the ISM usually consists of three distinct phases, a cold neutral phase, a warm phase that is both neutral and ionized, and a hot ionized phase. These phases are additionally in pressure equilibrium (McKee and Ostriker [1977]).

This can be fairly easily explained by taking a closer look at the mechanisms that determine the temperature of the diffuse gas in a galaxy. The gas is heated by photoelectric ionization of grains by ultraviolet photons (Bakes and Tielens [1994]), ionization by cosmic rays (Blandford and Ostriker [1980]), soft X-rays (McCammon and Sanders [1990]), and other mechanisms (Hollenbach and McKee [1989]). Cooling takes place due to collisional excitation of fine structure lines (Launay and Roueff [1977]), electron recombination(Bakes and Tielens [1994]), and other processes (Hollenbach and McKee [1989]). The efficiency of both heating and cooling generally depends on the composition of the ISM and its density and temperature (Wolfire et al. [1995]). A simple parametrisation of the temperature change in a volume element of the ISM would be

$$\mathrm{d}T = n\Gamma - n^2\Lambda, \tag{1.48}$$

where Γ is the heating rate, and Λ is the cooling rate, both of which might be functions of temperature. It is now obvious to see that an equilibrium temperature will be obtained for

$$\Gamma = n\Lambda. \tag{1.49}$$

This equilibrium temperature will depend on density and furthermore, since pressure $p = nT$ will correspond to an equilibrium pressure that will be sensitive to the exact form of the cooling and heating rates, respectively. This dependency can now be turned around by assuming that pressure will be set by the surroundings of the volume element. Thus, for a given pressure there might be more than one viable pairing of density n and temperature T, that satisfies the equilibrium condition. This concept is illustrated in figure 1.2 (Wolfire et al. [1995]), where it can be seen that starting on a point on the downwards slope of the line of stability, small perturbations in density are intensified and the system is pushed towards the regions of upwards slope. There are even more mechanisms that determine the behaviour

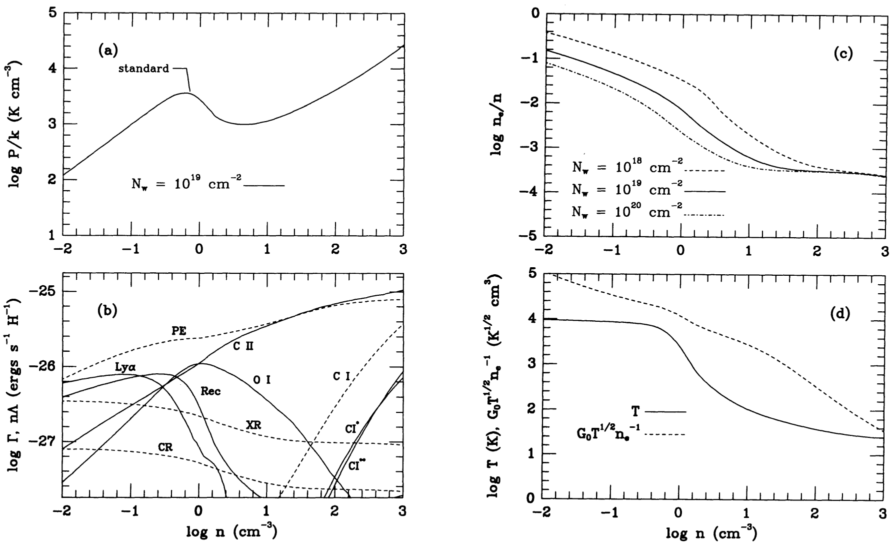

Fig. 1.2: (a)Thermal pressure versus hydrogen density. (b)Heating(dashed) and cooling(solid)rates per nucleus versus hydrogen density. (c)Electron fraction versus hydrogen density. (d)Gas temperature(solid) and ionization parameter (dashed) as a function of hydrogen density. Taken from (Wolfire et al. [1995])

of the ISM, like magnetic fields, that go above the scope of this work and are not relevant for the numerical simulations described later.

1.4 Molecular Clouds

Looking at the distribution of hydrogen in the Milky Way, one finds that molecular hydrogen is predominantly clumped together into cloud-like objects, with extensions of tens to hundreds of parsec and masses ranging from several thousands to millions of $M_\odot$ (e.g. Table I from (Heyer et al. [2009])). These molecular clouds are the densest regions in the ISM and have long been associated with star formation. To get a feeling for whether and how these clouds might collapse under gravitation, we once more look at the Euler equation, this time in three dimensions:

$$\rho \frac{\partial \boldsymbol{v}}{\partial t} + \rho \left(\boldsymbol{v} \cdot \boldsymbol{\nabla} \right) \boldsymbol{v} = -\boldsymbol{\nabla} p - \rho \boldsymbol{\nabla} \Phi. \tag{1.50}$$

Once more we make an Ansatz for small perturbations $\delta\rho$, $\delta\boldsymbol{v}$, and $\delta\Phi$:

$$\rho = \rho_0 + \delta\rho \cdot \exp\left[i \left(\boldsymbol{k} \cdot \boldsymbol{r} - \omega t \right) \right] \tag{1.51}$$

$$\boldsymbol{v} = \delta \boldsymbol{v} \cdot \exp\left[i\left(\boldsymbol{k} \cdot \boldsymbol{r} - \omega t\right)\right] \tag{1.52}$$

$$\Phi = \delta \Phi \cdot \exp\left[i\left(\boldsymbol{k} \cdot \boldsymbol{r} - \omega t\right)\right]. \tag{1.53}$$

We use the isothermal equation of state

$$p = c_s^2 \rho. \tag{1.54}$$

Plugging these into equation 1.50 and omitting terms of order greater than one, we get

$$-\mathrm{i}\omega\rho_0\delta\boldsymbol{v} = -\mathrm{i}\boldsymbol{k}c_s^2\delta\rho - \mathrm{i}\boldsymbol{k}\rho_0\delta\Phi. \tag{1.55}$$

We now multiply both sides with $\mathrm{i}\boldsymbol{k}$ to get

$$\omega\rho_0\delta\boldsymbol{v} \cdot \boldsymbol{k} = c_s^2 k^2 \delta\rho + k^2\rho_0\delta\Phi. \tag{1.56}$$

Using the Poisson equation we can relate the potential to the density:

$$\delta\Phi = \frac{4\pi G}{k^2}, \tag{1.57}$$

and arrive at

$$\omega\rho_0\delta\boldsymbol{v} \cdot \boldsymbol{k} = c_s^2 k^2 \delta\rho - \rho_0 4\pi G \delta\rho. \tag{1.58}$$

Now we have a look at the continuity equation

$$\frac{\partial \rho}{\partial t} = \boldsymbol{\nabla}\left(\rho \boldsymbol{v}\right). \tag{1.59}$$

Using our ansatz this can be derived to be

$$\omega^2\delta\rho = \omega\rho_0\delta\boldsymbol{v} \cdot \boldsymbol{k}. \tag{1.60}$$

Since the left side of equation 1.56 and the right side of equation 1.60 are equal, this leads to

$$\omega^2 = c_s^2 k^2 - 4\pi G\rho_0. \tag{1.61}$$

For an exponential growth, the right side of this equation has to be negative, hence the wavenumber k has to be smaller than

$$k_0 = \left(\frac{4\pi G\rho_0}{c_s^2}\right)^{\frac{1}{2}}. \tag{1.62}$$

The relation $k = \frac{2\pi}{\lambda}$ gives us a typical length-scale for growing perturbations, the so-called Jeans length

$$\lambda_J = \left(\frac{\pi c_s^2}{G\rho_0}\right)^{\frac{1}{2}}, \tag{1.63}$$

which then allows us to estimate the mass, above which a cloud should be unstable against gravitational collapse, the Jeans mass

$$M_J = \rho_0 \lambda_J^3 = \frac{\pi^{\frac{3}{2}} c_s^3}{G^{\frac{3}{2}} \rho_0^{\frac{1}{2}}}, \tag{1.64}$$

which for the dense molecular regions in the ISM is of the order of a few solar masses. Clouds with a mass exceeding the Jeans mass will collapse on a time scale

$$\tau = \frac{1}{\sqrt{4\pi G \rho_0}}, \tag{1.65}$$

which is of the order of some million years for molecular clouds.

This gives rise to a certain problem. Almost all molecular clouds in the Milky Way Galaxy should be Jeans unstable. With about $10^9 M_\odot$ of hydrogen in the galaxy, this should lead to a star formation rate of

$$\left(\frac{\mathrm{d}M_*}{\mathrm{d}t}\right) = \frac{M_{H2}}{\tau} = \frac{10^9 M_\odot}{10^6 yr} = 10^3 \frac{M.}{yr}. \tag{1.66}$$

The observed star formation rate in the Milky Way is only $1{-}3 M_\odot/yr$, however. This begs the question as to why hydrogen seems to collapse slower than it is expected to (Zuckerman and Evans [1974]). Many ideas have been brought forth to explain this discrepancy, from turbulence (Krumholz et al. [2006]) to magnetic fields (Shu et al. [2007]) and the fact that molecular clouds are not actually gravitationally bound (Dobbs et al. [2011a]). Also, non-linear perturbations lead to cores that are much more dense and collapse faster than the rest of the cloud, turning a small percentage of the cloud into stars, the feedback of which potentially disrupts the cloud (Vázquez-Semadeni et al. [2007]).

1.5 Star Formation & Stellar Feedback

Further investigation of the star forming process is warranted. There are many micro-physical properties involved, such as turbulence, gravity, and magnetic fields. Turbulence can both slow down collapse, or facilitate it, depending on its exact nature in a given system. It is also not clear beyond doubt how turbulence is driven and sustained over many dissipation timescales. Magnetic fields might hold the answers to that but investigating them is very complex, both in observations and simulations. The gravitational behaviour then strongly depends on the density structure imposed by the turbulence.

Also, the star formation itself is expected to have a strong influence on the star forming ISM, via feedback processes. First and foremost, stars emit radiation that strongly heats and ionizes the gas surrounding them. Most stars also eject particle winds that transfer further energy to the ISM and generate shock fronts. Also, massive stars only live for short times before exploding in supernova events that deposit enormous amounts of energy and material back into the galaxy. Stars are furthermore crucial in creating and enriching the ISM with metals and heavier atoms that form the basis for the formation of dust particles that are so crucial for its energy budget. One can easily see that the precise treatment of all this goes far beyond the scope of this work.

Indeed, when observing galaxies one can find a large range of different regimes of star formations. From ellipticals with almost none, over extended galactic disks with star formation rates of several $M_\odot$ per year, up to star bursts with up to $1000 M_\odot$ per year. While these regimes surely have individual causes, be it accumulation in spiral shocks, or funnelling of gas by central bars, or major mergers, there is nevertheless a strong correlation between star formation and molecular hydrogen. This is evident in the so-called Kennicutt-Schmidt law of star formation (Kennicutt [1998], Schmidt [1959]), illustrated in figure 1.3. It states that the surface density of the star formation rate for any region is determined by its surface density of molecular hydrogen:

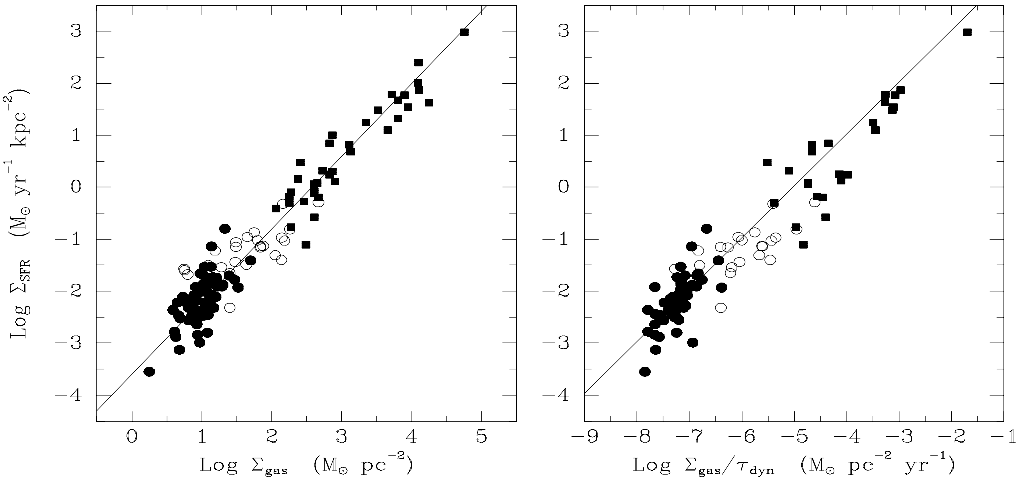

Fig. 1.3: Left side: Star formation density plotted against gas density. Solid points denote normal spirals, squares denote circumnuclear starbursts, circles denote inner regions of normal disks. Right side: Same data plotted against the ratio of the gas density to the orbital time in the disk. (Taken from (Kennicutt [1998]))

$$\Sigma_{SFR} \propto \Sigma_{H2}^{N}. \tag{1.67}$$

The exponent N can range from 1 to 1.4, depending on the method of measuring the density that is used (Krumholz and Thompson [2007]). One also finds a tight correlation between the star formation density and the ratio of the gas density to the orbital time

$$\Sigma_{SFR} \propto \frac{\Sigma_{H2}}{\tau_{dyn}}, \tag{1.68}$$

which holds independently from the tracers used to determine star formation rates or gas densities.

1.6 Gas Accretion

This relation between the star formation rate and the gas content in a galaxy begets the assumption that there should also be a link between star formation and the accretion of new gas into said galaxy. Accretion rates have the disadvantage of being incredibly hard to measure observationally and even simulations are just now getting to the point of being able to determine them. To make some first assertions as to the connection between the two, we look at a very basic model (Bouché et al. [2010]). Namely we treat the mass of hydrogen as a reservoir that evolves according to

$$\dot{M}_{gas} = \dot{M}_{acc} - \alpha \cdot SFR, \tag{1.69}$$

where $\dot{M}_{gas}$ is the time derivative of the gas mass, $\dot{M}_{acc}$ is the cold gas accretion rate, and α is a proportionality factor, caused by the fact that a fraction of the gas that is depleted by star formation is recycled into the galaxy and stellar feedback leads to a certain amount of outflow of gas from it. To determine the SFR we use the Kennicutt-Schmidt relation, that can be shown to be of the universal form

$$SFR = \frac{\epsilon_{SFR}}{t_{dyn}} M_{gas}. \tag{1.70}$$

This implies that a system transforms a certain fraction ϵ_{SFR} of its hydrogen gas into stars over one dynamical time t_{dyn}. This allows us to write equation 1.69 as

$$\dot{M}_{gas} = \dot{M}_{acc} - \frac{\alpha \epsilon_{SFR}}{t_{dyn}} M_{gas}. \tag{1.71}$$

This differential equation can be solved if the time dependence of M_{gas} is of the form

$$M_{gas}(t) = \frac{t_{dyn} \dot{M}_{acc}}{\alpha \epsilon_{SFR}} - C \cdot exp\left(1 - \frac{\alpha \epsilon_{SFR}}{t_{dyn}} t\right), \tag{1.72}$$

where C is an integration constant determined by the initial conditions. Figure 1.4 illustrates the general behaviour of $M_{gas}(t)$, namely that for large t it approaches a constant equilibrium value. This equilibrium value is in our specific case determined to be

$$M_{gas} \to \frac{t_{dyn} \dot{M}_{acc}}{\alpha \epsilon_{SFR}}. \tag{1.73}$$

In other words, the system reaches an equilibrium state, where $\dot{M}_{gas}$ is zero and the star formation rate

$$\boxed{SFR = \frac{1}{\alpha} \dot{M}_{acc}}, \tag{1.74}$$

is directly set by the accretion rate. Of course, all this is only valid if the accretion rate doesn't change over the timescale needed to reach this equilibrium state. Figure

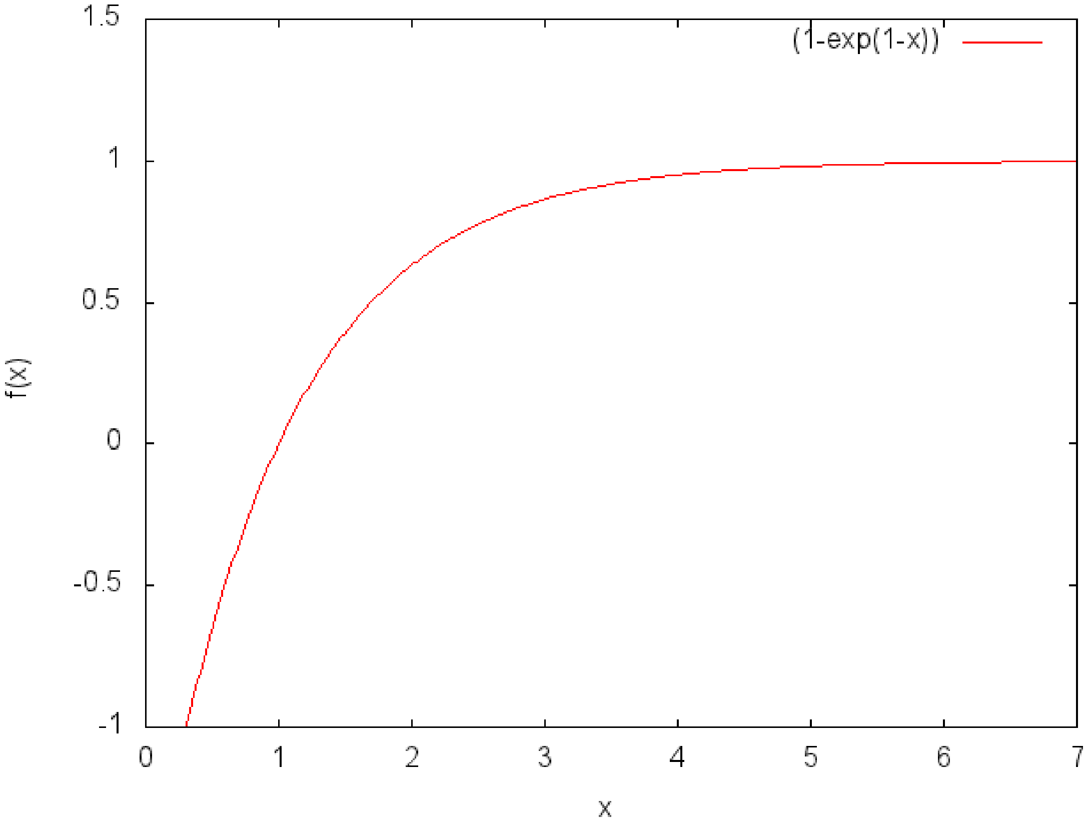

Fig. 1.4: Illustration of the behaviour of the function $(1 - exp(1 - x))$ from equation 1.72.

1.5 shows that this simple toy model can indeed give this expected behaviour if it is numerically solved for long times, even taking into account accretion rates that change with redshift.

It should again be noted that this is a very simplistic model. In reality, it seems highly likely that not only the net accretion rate but also the mode of accretion, whether it be hot or cold gas, whether the densities of accreted gas are significantly higher or lower than those of the disk material, should have a considerable impact (Dekel et al. [2009], Genel et al. [2012]).

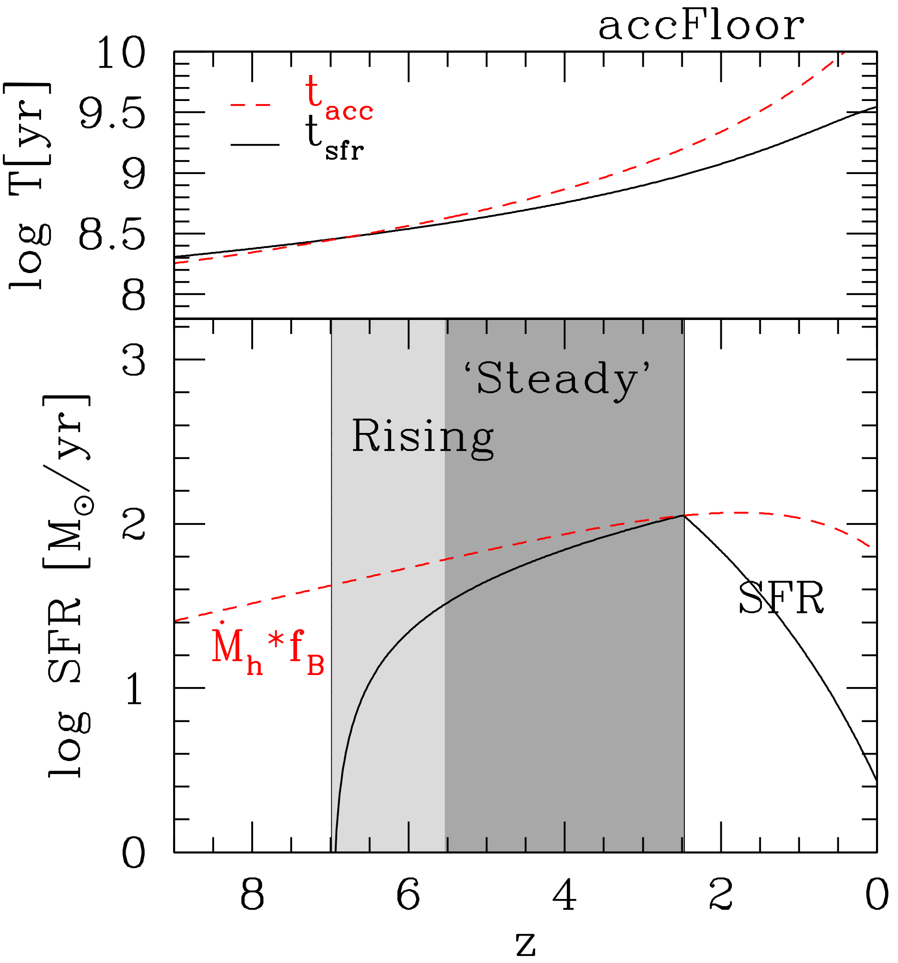

Fig. 1.5: Top panel: Accretion (red dashed) and SFR (solid black) timescales versus redshift. Bottom panel: SFR (solid black) and maximum accretion rate (red dashed) against redshift. It can be seen that the SFR reaches a quasi-steady state, where the SFR follows the accretion rate. Taken from (Bouché et al. [2010])

2 Numerical Implementation

2.1 Hydrodynamic Code GADGET3

For this work we use the cosmological simulation code GADGET3, which is based on the publicly available version GADGET-2 (Springel [2005]), commonly used for simulations of Dark Matter structure formation and evolution of galaxies. The additional implementation of many supplemental features by different groups allows the study of a variety of different physical systems. The code was written in C and uses both the MPI and the OpenMP libraries for parallelisation.

GADGET3 uses smoothed particle hydrodynamics(SPH) to solve the equations of motion for an ideal gas, using a smoothing kernel that uses adaptive smoothing lengths without giving up conversation of both energy and entropy in the system. It also introduces an artificial viscosity to better deal with contact discontinuities, e.g. in shocks, which is traditionally a problem when using SPH-methods. To calculate gravitational forces, the code employs a monopole expansion in an oct-tree approach for grouping the particles, in an effort to allow maximum parallelisation with minimum memory requirements at short distances and switches to Fourier techniques for evaluating gravity at long ranges.

The parameters and routines used in any one run are set by modifying the Makefile and a separate parameter file. For initial conditions, the number of particles needs to be clarified, each one with a mass, initial positions, velocities, and specific internal energies.

2.2 Additional Physics

2.2.1 Galactic Potential

In order to get the correct form for densities and rotation curves in a computationally less expensive manner, we omit explicitly treating dark matter, but instead opt to assign the simulated particles an additional acceleration. We take an acceleration corresponding to a logarithmic potential

$$\Phi_L = \frac{1}{2} v_0^2 \ln\left(R_c^2 + R^2 + \frac{z^2}{z_q^2}\right), \tag{2.1}$$

where v_0 and R_c are constants and z_q is the axis ratio of the equipotential surfaces(Binney and Tremaine [2008]).

We also incorporate a potential for rotating spiral density perturbations, taken from (Cox and Gómez [2002]).

2.2.2 Cooling

For the cooling we use the simple equation 1.48, where we assume

$$\Gamma = 2.0 \cdot 10^{-26} (ergs/s) \tag{2.2}$$

to be constant, and $\Lambda(T)$ is calculated to be

$$\Lambda(T) = \Gamma \cdot (f_1 + f_2)\, cm^3, \tag{2.3}$$

where

$$f_1 = 1.0 \cdot 10^7 \cdot \exp\left(\frac{-1.184 \cdot 10^5}{T + 1000.0}\right), \tag{2.4}$$

and

$$f_2 = 1.4 \cdot 10^{-2} \sqrt{T} \exp\left(-\frac{92.0}{T}\right). \tag{2.5}$$

This is taken from (Vázquez-Semadeni et al. [2007]). The thermal pressure is illustrated in figure 2.1. Comparison to figure 1.2 shows that this cooling procedure should yield a stable two phase medium.

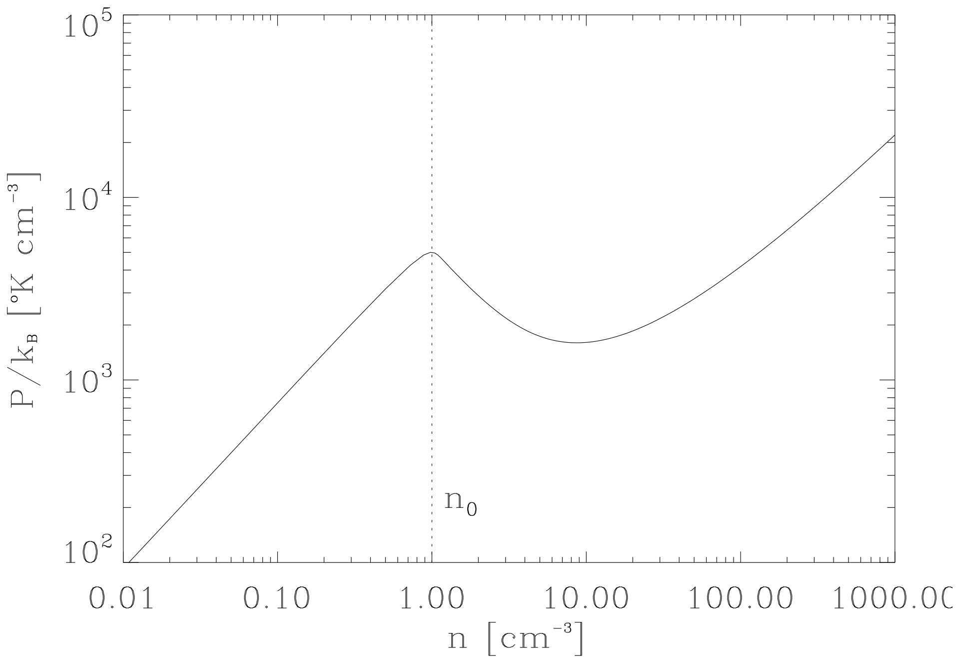

Fig. 2.1: Thermal equilibrium pressure versus density for the heating and cooling prescription used throughout this work. Taken from (Vázquez-Semadeni et al. [2007]). The vertical line denotes the initial density (Vázquez-Semadeni et al. [2007]) used in their work.

The numerical implementation goes as follows. Each timestep we loop over all active particles. For each particle, we determine the internal thermal energy u, density ρ, and its assigned timestep dt. We calculate the temperature corresponding to the thermal energy and use these values to determine the change in energy due to cooling by radiation, du_{rad}, to be

$$\mathrm{d}u_{rad} = \Lambda(T)\frac{n^2}{\rho}\mathrm{d}t, \tag{2.6}$$

where n is the particle density, assuming a molecular weight for the gas

$$\mu = 1.27 m_p, \tag{2.7}$$

m_p donating the proton mass, and $\Lambda(T)$ according to equation 2.3 We refine this cooling by setting a limit on what fraction of the initial thermal energy can be radiated at once at constant cooling rate. Should the change exceed this limit, the thermal energy is reduced by this fraction and the time needed for that is determined. Then a new cooling rate is calculated for this lowered temperature and the amount of energy radiated away in the remainder of the timestep is determined. This refinement is repeated as necessary, until the end of the timestep is reached.

After that we add to the internal thermal energy a value due to heating, that is calculated to be

$$\mathrm{d}u_{heat} = \Gamma \mathrm{d}t, \tag{2.8}$$

with Γ taken from equation 2.2.

2.2.3 Star formation and stellar feedback

The basis for our star formation and stellar feedback implementation is taken from (Dobbs et al. [2011b]). To determine star forming events in this model, we first loop through all particles, checking whether their SPH density is over a certain threshold. For each of these particles, we then consider a sphere with pre-set radius around it and find all SPH particles therein. We use this information to calculate the centre of mass and the total number of particles and mass inside that sphere. For star formation, we assume that a certain fraction of the mass involved turns into stars. We then use this mass to calculate the amount of energy put into the remaining gas via supernova feedback, using

$$E_{SN} = \frac{\epsilon M_{H_2}}{160} 10^{51} ergs, \tag{2.9}$$

where ϵ is the fraction of hydrogen mass turned into stars and we assume that one supernova event will happen for each 160 solar masses of stars formed, each supernova contributing $10^{51} ergs$ of energy to the feedback. We consider both kinetic and thermal feedback. For the kinetic feedback we add to the present velocity a value corresponding to the total energy of all super novae distributed across the ambient medium and scaled to the distance of the particle to the centre of the event. For the thermal feedback, we calculate the temperature of the ambient medium and set the internal energy of affected particles to the corresponding value.

We modified the model by introducing a subroutine that turns gas particles into star particles, in order to decrease the total gas mass in the disk, according to equation 1.69. To do this we determine the number of particles participating in a star forming event in addition to their total mass. We then select the fraction ϵ of these particles at random, so that we remove the right amount of gas mass, where we exclude the central particle, and set their mass to zero, so that GADGET can then at a later point remove these particles from the simulation in a numerically correct way. Also, setting the mass to zero removes the particles from the SPH-calculations, so they no longer impact the physics of the system in any way. Finally we transform the central particle into a star particle, with a mass equal to the cumulative mass of all particles removed that way.

2.2.4 Injection of new gas particles

To simulate the accretion of new gas, we utilise a very crude routine that can easily be modified and extended should one be interested in a more physical approach of handling accretion. First we set an arbitrary accretion rate. Then we calculate every timestep, how many particles should have been created with this particular rate. This number is determined using non-integer values, since for small timesteps, a low number of particles, or low accretion rates, less than one particle would be created per timestep. The values are then summed up over time.

Once we reach a value bigger than one, we start the injection routine, decreasing the value of accreted particles by one in each iteration. The first step of the routine is determining a position for the new particle. This is done in one of two ways: either we pick a distance to the rotation axis at random, distributed exponentially with a scale radius of $4kpc$, where we forbid injection in the innermost $2kpc$ in order to prevent the majority of new particles to be created in the region of highest density. Alternatively we choose the radius to be uniformly between nine and ten kpc. We set the distance to the equatorial plane to be exponentially distributed, with a scale height of $200pc$, again forbidding the innermost $50pc$. Next we search the nearest particle to that position in order to know on which process to inject the new particle.

To insert a new particle into a running simulation is a non-trivial task. To implement it, we raise the variables denoting SPH-particle number and total particle number by one, thus gaining acces to memory space in the particle sequence that GADGET has already allocated to this task to be able to manage fluctuations in particle number due to fluctuating distribution of particles between individual processes. This allows us to copy the particle data structure of the first non-SPH particle, which is at this point stored in a slot reserved for SPH particles due to the increase in numbers, to the newly created and therefore vacant position in the particle sequence. If the simulation does not have non-SPH particles, this peculiar step will simply do nothing. Now we can copy the data structure of the determined closest particle into the memory slot of the formerly first non-SPH particles that will subsequently be treated as the last SPH particle in the sequence. Of course we also change the position variables to the position of the new particle and give it a new and unique identification number in order to later be able to trace the particles injected by this routine. So far this routine only works for setups that only allow one type of non-SPH particle, like the ones presented later in this work. If one was interested in running more elaborate simulations, one would have to modify the code appropriately.

3 Simulations

3.1 Numerical Tests

Before doing the high resolution simulations to test the hypotheses above, we performed a series of low resolution runs in which we tested the individual parts of our code. Each run was performed with an initial number of 100000 particles, which could increase or decrease with time due to accretion and star formation, respectively. For all following simulations we used a set of arbitrarily chosen code units to make sure that the floating point operations are done with numbers that are not exorbitantly large nor small. These units can be found in table 3.1, all other units are then derived from these.

Tab. 3.1: Code Units

unit_ length_ in_ cm	$100pc$
unit_ mass_ in_ g	$10^5 M_\odot$
unit_ velocity_ in_ cm_per_ s	$2.0747559 \cdot 10^5 \frac{cm}{s}$

3.1.1 Setup

To set up the initial conditions, we distributed the particles uniformly over a cylindrical disk with radius $10kpc$ and height $400pc$. The density profiles described in chapter 1.1 will evolve naturally over time, given the methods shown in chapter 2.2.1. We set an initial uniform density for the gas that gives us a total mass of $2.5 \cdot 10^9 M_\odot$. For an initial velocity, we take the circular velocity corresponding to the logarithmic part of the potential of equation 2.1, and superimpose a Gaussian random distribution with width $5km/s$. As a starting temperature for the particles we choose $700K$, which has shown to be irrelevant after letting the system evolve for several Myr. This is due to the fact that for the initial density, the cooling or heating time scales are so short that the gas takes on the equilibrium temperature before the initial temperature has a chance to affect the uniformity. For the cooling, we also generally us a minimum temperature floor of $500K$. We set the number of SPH-neighbours inside one smoothing length to be 40.

We made overall three test runs, one for cooling, one for star formation, and one for accretion, respectively. The exact physical processes used in each one are listed in table 3.2. For testing the accretion routine, we set the accretion rate to be $5M_\odot/yr$

Tab. 3.2: Processes used in Test Simulations

Simulation	Cooling	Star Formation	Accretion
Cooling	yes	yes	yes
Self-Gravity	no	yes	no
Star Formation	no	yes	no
Accretion	no	no	yes

and used the version that creates particles at exponentially distributed radii.

3.1.2 Cooling

Figure 3.1 shows the surface density for the run with only cooling at times $50 Myr$, $100 Myr$, $150 Myr$, and $200 Myr$. It shows very nicely how dense gas is gathered in the spiral arms over time. Figure 3.2 shows the fractions of gas in the different phases developing over time. Even without self-gravity of the particles, a significant amount of the gas gets cooled down to temperatures for which star formation would be possible. Gravity is even expected to increase this effect. We designate gas with a temperature below $1000 K$ as cold, gas with a temperature above $8000 K$ as hot, and gas with intermediate temperatures as warm. Figure 3.3 shows the Toomre Q parameter for different regions of the disk after $200 Myr$. It once more details that the material inside the spiral arms is in a state that allows gravitational collapse to be amplified.

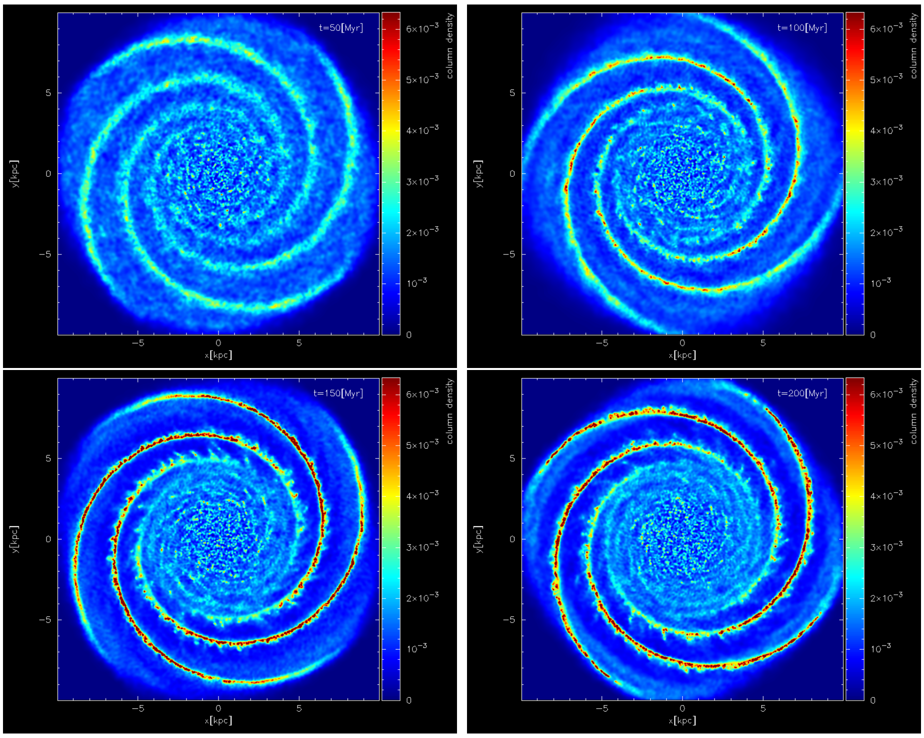

Fig. 3.1: Column densities in the disk for the test simulation including only cooling after (top left) $50 Myr$, (top right) $100 Myr$, (lower left) $150 Myr$, and (lower right) $200 Myr$.

3.1.3 Star Formation

Figure 3.4 shows the surface density for the star forming simulation at times $50 Myr$, $100 Myr$, $150 Myr$, and $200 Myr$. The stellar feedback disrupts the spiral arms and

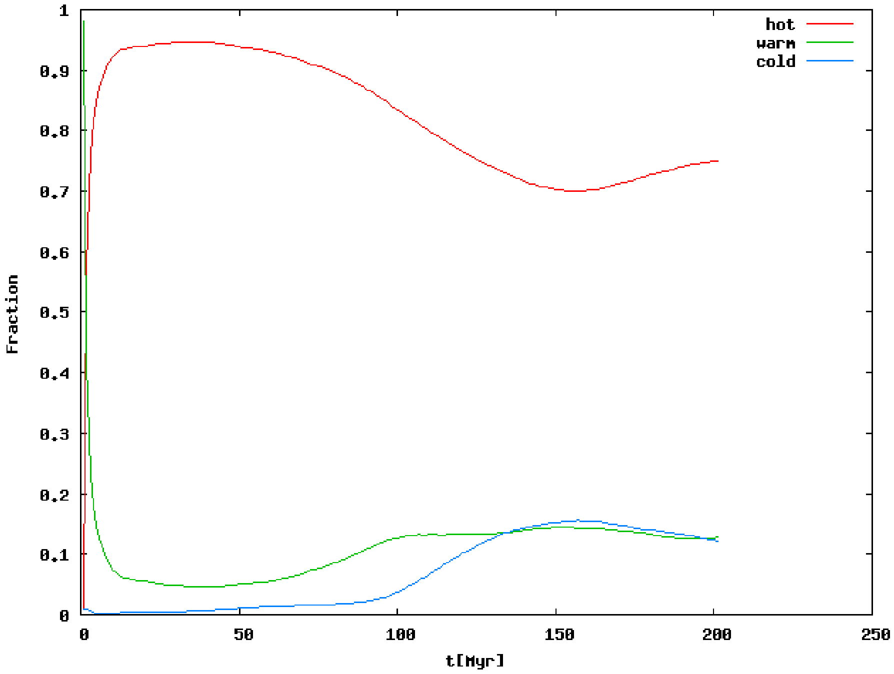

Fig. 3.2: The fractions of hot (red), warm (green, and cold(blue) gas in the ISM versus time for the test simulation including star formation.)

leads to a much more turbulent density distribution. Figure 3.5 shows the star formation rate density over time. It can be seen that the gas takes some time to cool down and get dense enough to form stars. The follows a rise in star formation before feedback can disrupt the cooling process enough to see a small drop and then there is an equilibrium state where the SFR is roughly constant. These values are comparable to those found in (Dobbs et al. [2011b]). Figure 3.6 shows the fractions of gas in the different phases developing over time. Again this figure shows us how the fraction of cold gas slowly builds up over time until star formation sets in. Afterwards the ISM reaches an equilibrium between cooling and heating by stellar feedback. Figure 3.7 shows the velocity dispersion in z-direction against time. We again see values comparable to those from (Dobbs et al. [2011b]). Also, the onset of star formation clearly drives turbulence, which we would expect from 3.1. Figure 3.8 shows the Toomre Q parameter for different regions of the disk after $200Myr$. We see clearly once more how the spiral arms are broken up by feedback and also that there are now regions with $Q < 1$ in between the spiral arms. These are compact objects that are blown out of the spiral by stellar feedback and can survive surrounded by the hot medium for quite some time.

3.1.4 Accretion

Figure 3.9 shows the surface density for the star forming simulation at times $50Myr$, $100Myr$, $150Myr$, and $200Myr$. The most significant difference to the other runs

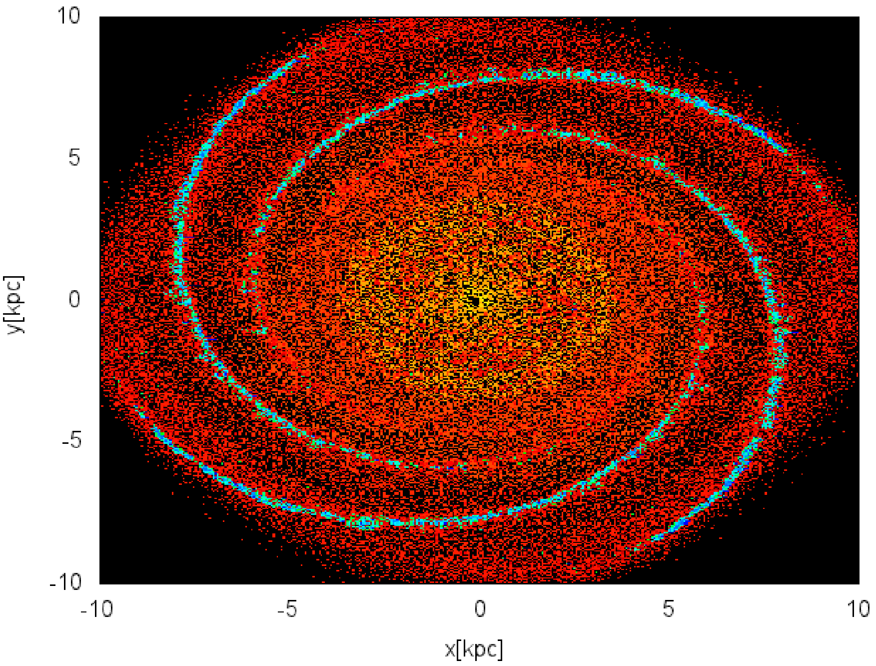

Fig. 3.3: Toomre stability parameter for the test simulation including only cooling. Blue colours denote regions with $Q < 1$, red colours denote areas with $Q > 1$.

is the formation of a ring-like structure. This is a consequence of the exponentially distributed radii of our injected particles, which leads to the majority of new gas being created at $R \sim 2kpc$. Figure 3.10 shows the fractions of gas in the different phases developing over time. The increase in cold gas, compared to the run with only cooling, is easily explained by the increase in density due to the higher number of particles. Higher density means more efficient cooling, which naturally leads to more cold gas. Figure 3.11 shows the velocity dispersion in z-direction against time. The velocity dispersion is what we would expect for a calculation without stellar feedback, compared to the first $50Myr$ of figure 3.7. This means that the newly injected gas does not disturb the dynamics of the disk in any meaningful way, but should be well incorporated into it. Figure 3.12 shows the Toomre Q parameter for different regions of the disk after $200Myr$. It looks very much like figure 3.3, except for a region of marginal instability where we inject the majority of our particles. Figure 3.13 shows the number of SPH-particles in our simulation over time. It is fairly obvious that the number increases in a linear fashion. The slope of the line is $5M_{\odot}/year$, the predefined value. We can be certain that our routine will create the exact right amount of particles that we want.

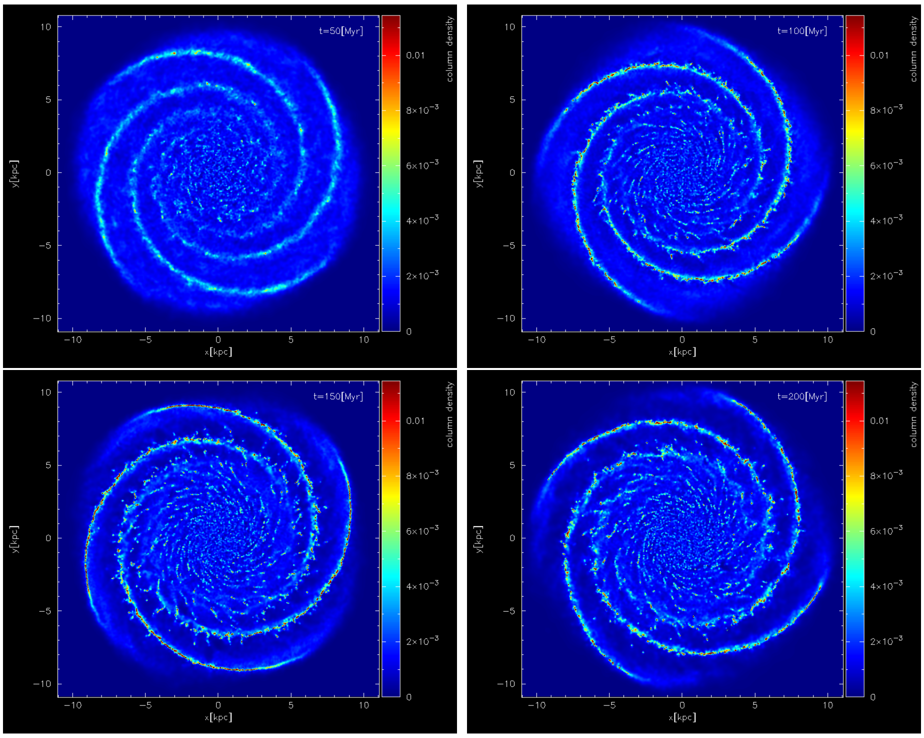

Fig. 3.4: Column densities in the disk for the test simulation including star formation after (top left) $50 Myr$, (top right) $100 Myr$, (lower left) $150 Myr$, and (lower right) $200 Myr$.

3.2 Star Formation & Gas Accretion

3.2.1 Setup

To test the assumptions gleaned from chapter 1.6, we set up a high resolution simulation in which we make use of all our routines described in chapter 2. We started with eight million particles, set up as in chapter 3.1.1, except that we gave them an initial temperature of $5000K$, and we left an empty space in the center of the disk with a radius of $2kpc$. The initial temperature should not make any difference, as detailed earlier. We chose to keep the central parts of the disk empty to save computational resources and are not particularly interested in these regions, since most star formation happens in the spiral arms that don't reach that far inward. And although we assume particles to travel into the centre, according to (Krumholz and Burkert [2010]), we have found that for the calculated time intervals, this effect only plays a minor role. It should be noted here that we face a resolution problem, since according to (Bate and Burkert [1997]) we would need many more particles to resolve the Jeans mass at our threshold density of $1000/cm^3$ at our minimum temperature of $500K$, but this resolution we have is the best we can do with the given computational resources, and we are better resolved than most studies that came before this work.

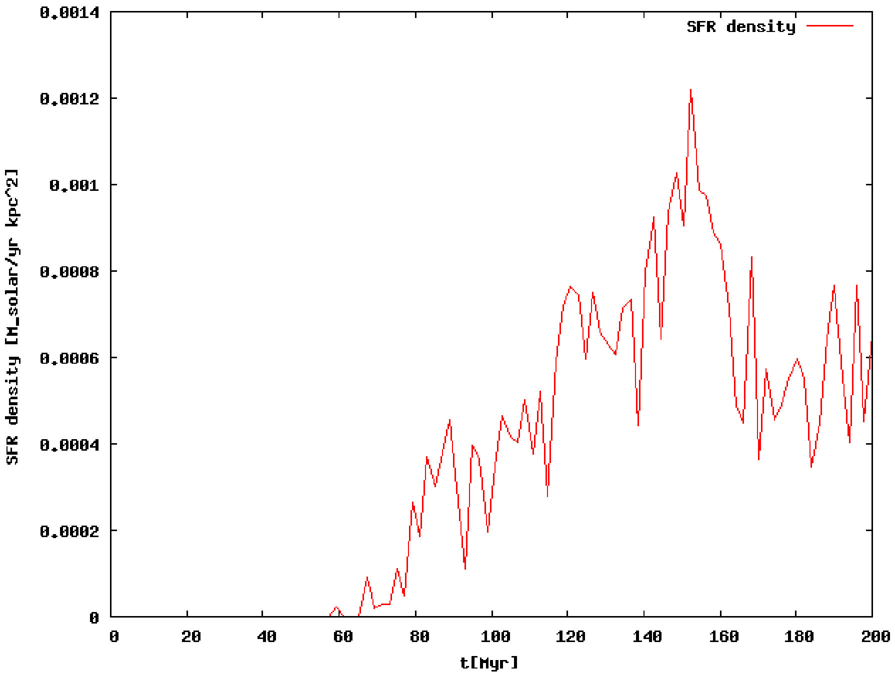

Fig. 3.5: Star formation rate density against time for the test simulation including star formation.

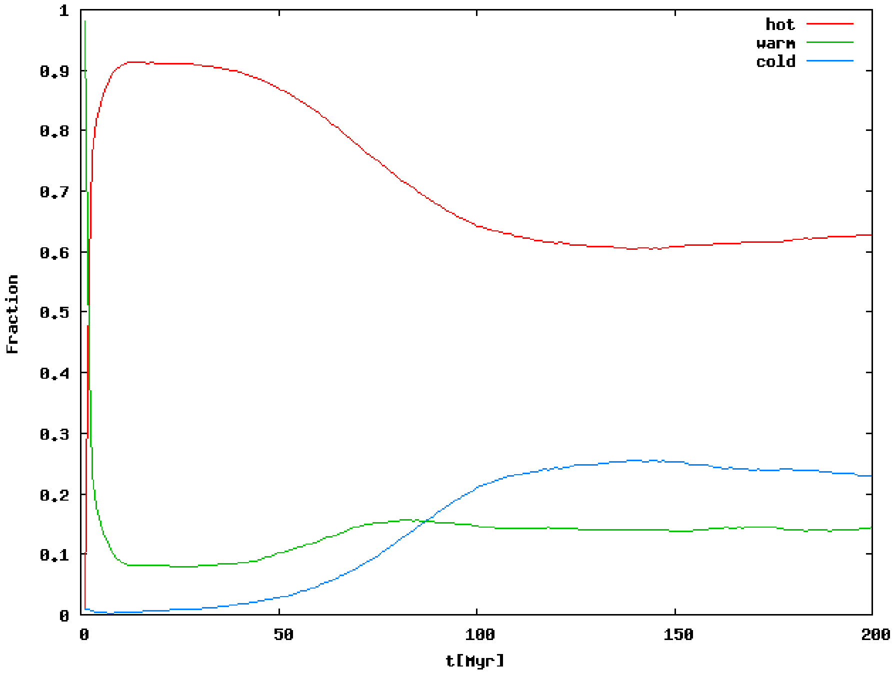

Fig. 3.6: The fractions of hot (red), warm (green, and cold(blue) gas in the ISM versus time for the test simulation including star formation.)

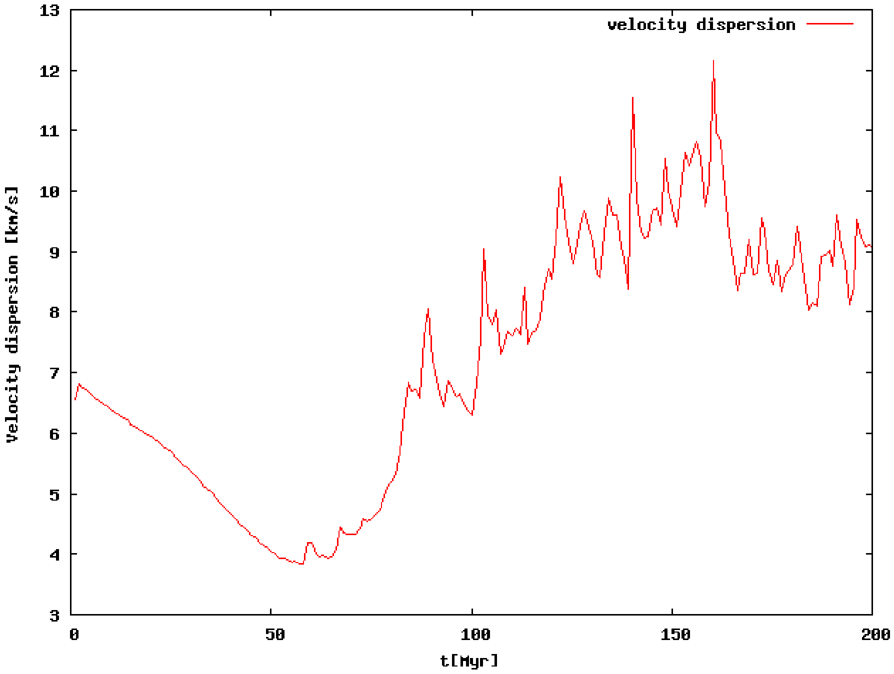

Fig. 3.7: Velocity dispersion in z-direction against time for the test simulation including star formation.

We executed this simulation in the following way. We evolved the highly resolved disk for $300Myr$, without gas accretion up to this point. After that we had to reduce the resolution even further due to time concerns. For that we took the final snapshot of the preceding simulations and selected 50% of the SPH-particles at random and multiplied their mass by a factor of two. We repeated this step a second time for a total particle number of approximately two million. We then took these new initial conditions and had two simulations running, one with each of our accretion schemes with an accretion rate of $20M_{\odot}/yr$. We let these systems evolve for $100Myr$ then we chose to continue with the EDGE-scheme, mostly because it is somewhat less computationally expensive. We started three more simulations, based on the end state of the previous one, and tried three different accretion rates. First we took an accretion rate that was equal to the star formation rate of that particular snapshot chosen as a new initial setup, in this case this means $\dot{M}_{acc} = 0.8M_{\odot}/yr$. For the second run we took an accretion rate that was two times as high, $1.6M_{\odot}/yr$, and for the last one we turned off accretion all together. We then let these systems evolve for $50Myr$ to see whether there would be any difference.

3.2.2 Results

Figure 3.14 shows the column density of the setup-run with eight million particles at the beginning, after $100Myr$, after $200Myr$, and after $300Myr$. It shows the highly turbulent structure of the ISM, with many transient features between the

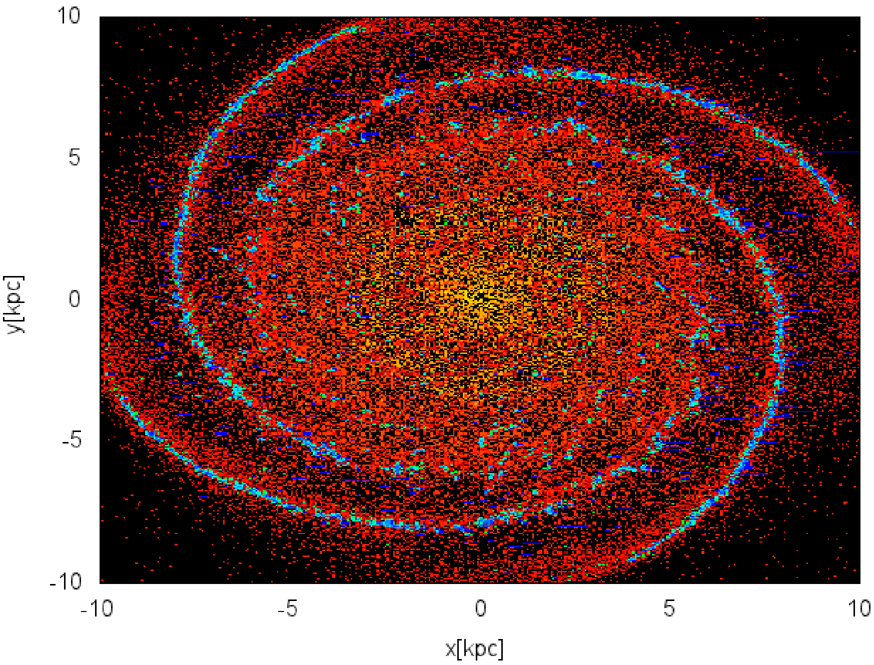

Fig. 3.8: Toomre stability parameter for the test simulation including star formation. Blue colours denote regions with $Q < 1$, red colours denote areas with $Q > 1$.

spiral arms. Figure 3.15 shows how the star formation rate evolves over time for this first run. It is comparable to 3.5, in that it shows an initial peak and then seems to reach somewhat of an equilibrium after 100Myr. The differences to 3.5 are due to the much higher resolution. Figure 3.16 then shows the star formation rates for the two runs with accretion over time. It can be clearly seen that the SFR rises linearly in time, as one would expect, since the total mass of the system also increases linearly. This shows nicely how the fresh supply of gas forces the SFR to rise and accommodate to the accretion rate, although we were not able to run the simulation long enough for a steady state to develop due to the time restraints given for this work. Also, there is no difference between the two accretion schemes concerning star formation, consistent with our somewhat simplistic model from chapter 1.6. The SFR rises very slowly, so it would take much more time than is reasonable for us to wait until an equilibrium might be reached. Figure 3.17 shows the column densities for the final states of the two high-accretion runs. The most notable feature is the ring of high density gas at the edge of the disk in the EDGE-accretion scheme. This is not unexpected, since we inject a lot of particles in this region, which take some time to be distributed over the disk, longer than the time for them needed to cool and collapse. This might skewer our results, but the fact that the exponentially distributed accretion scheme shows the same behaviour in the SFR gives us confidence that this would only have a minor influence. Figure 3.18 shows the column densities for our three comparison simulations after each

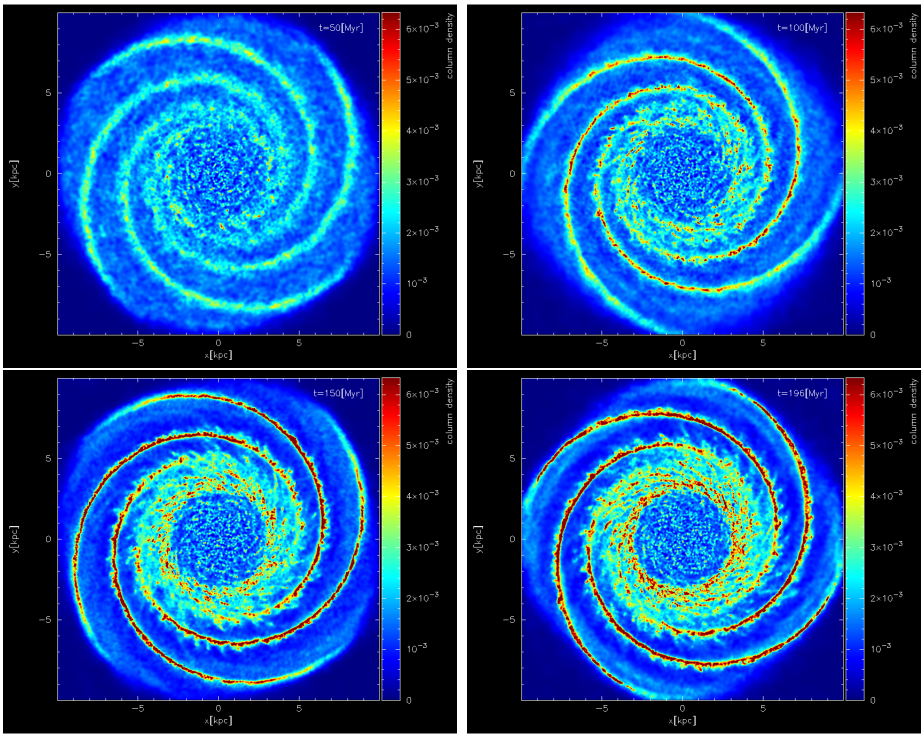

Fig. 3.9: Column densities in the disk for the test simulation including gas accretion after (top left) $50Myr$, (top right) $100Myr$, (lower left) $150Myr$, and (lower right) $200Myr$.

has evolved for some time The first thing that leaps to the eye is the fact that the outer ring seems to be breaking up now that it is no longer continuously fed at the high rate that built it up. This is consistent with chapter 1.2, where perturbations can freely grow. The rest of the disk is largely unaffected and does not show any signs of peculiar evolution. Figure 3.19 shows the star formation rates for our three simulations against time. No difference can be discerned between the three lines. On first glance one might assume that this is contradictory to what we said in chapter 1.6, where we claimed that the SFR will be determined by the accretion rate. However, one should not forget that it takes time to reach this quasi-steady state, a time comparable to $t_{dyn}/(\alpha\epsilon_{SFR})$. If we assume the dynamical time to be of the order of the depletion time $M_{gas}/SFR \sim 1Gyr$, α to be unity and the star formation efficiency $\epsilon_{SFR} \sim 10\%$, we would have to wait several Gyr for equilibrium to set in. This is consistent with the findings of (Bouché et al. [2010]), who had their systems evolve from a redshift of $z = 9$ forward. It is also clearly visible in figure 3.16, where it takes about $50Myr$ before a significant rise in SFR can be seen, the same amount of time the simulations in figure 3.19 actually ran.

This would mean that the disk is still trying to accommodate to an accretion rate of $20M_\odot/yr$ for the durations that we simulated. Our assumption is enforced by figure 3.20, where we plotted our expectation for the behaviour of the SFR according to chapter 1.6, for an accretion rate of $20M_\odot/yr$. We estimate the dynamical time

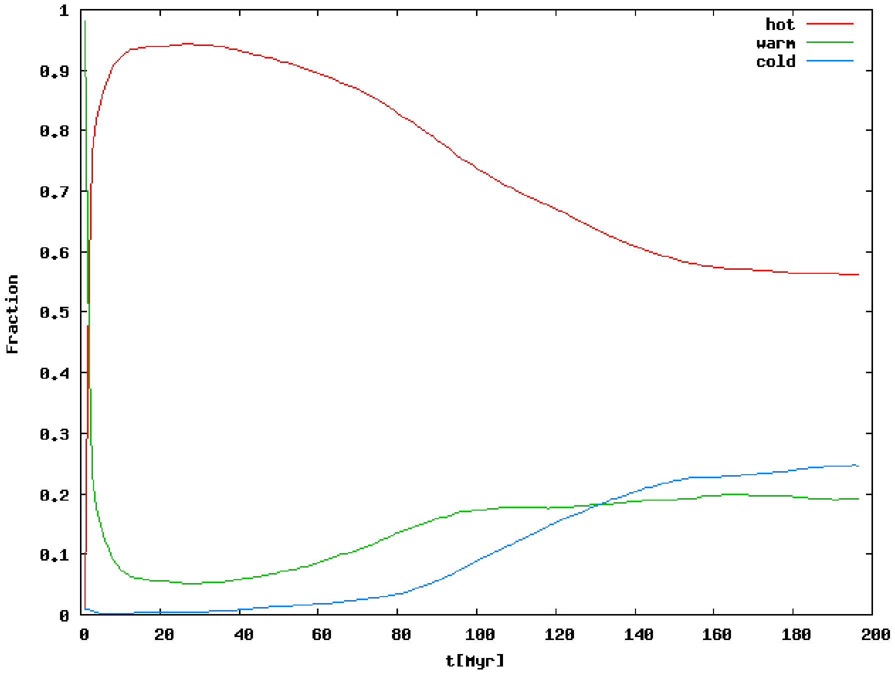

Fig. 3.10: The fractions of hot (red), warm (green), and cold(blue) gas in the ISM versus time for the test simulation including gas accretion.

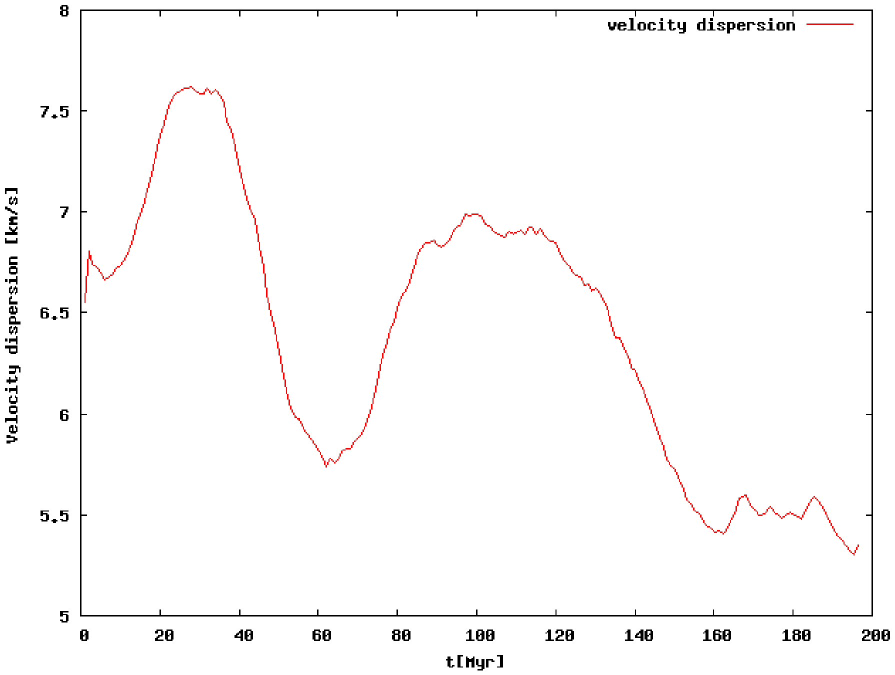

Fig. 3.11: Velocity dispersion in z-direction against time for the test simulation including gas accretion.

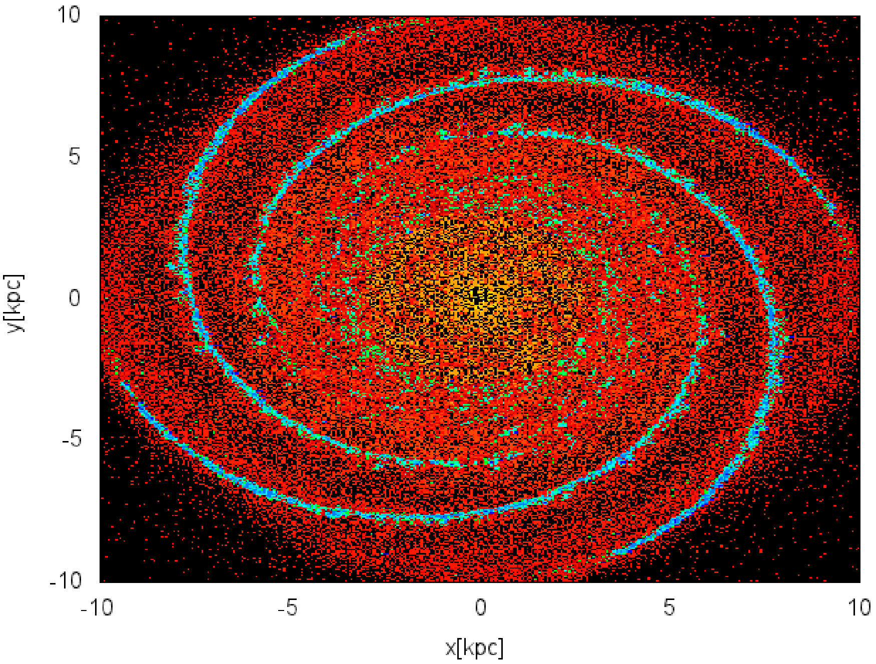

Fig. 3.12: Toomre stability parameter for the test simulation including star formation. Blue colours denote regions with $Q < 1$, red colours denote areas with $Q > 1$.

to be $1250 Myr$ and set the line so we would get an SFR of $0.25 M_\odot/yr$ at the time $60 Myr$. This gives us the function

$$SFR(t) = 20\frac{M_\odot}{yr} - \frac{19.75\frac{M_\odot}{yr}}{e} \cdot e^{1-\frac{t-60}{1250}}. \qquad (3.1)$$

Figure 3.20 shows nicely that even the runs with significantly lower accretion rates still follow the line given by an accretion rate of $20 M_\odot/yr$. Looking at figure 3.19, one might think that the SFRs for the low accretion and no accretion runs are about to drop or at least rise slower than the SFR of the high accretion run. Unfortunately this could not be further determined within the timeframe of this work.

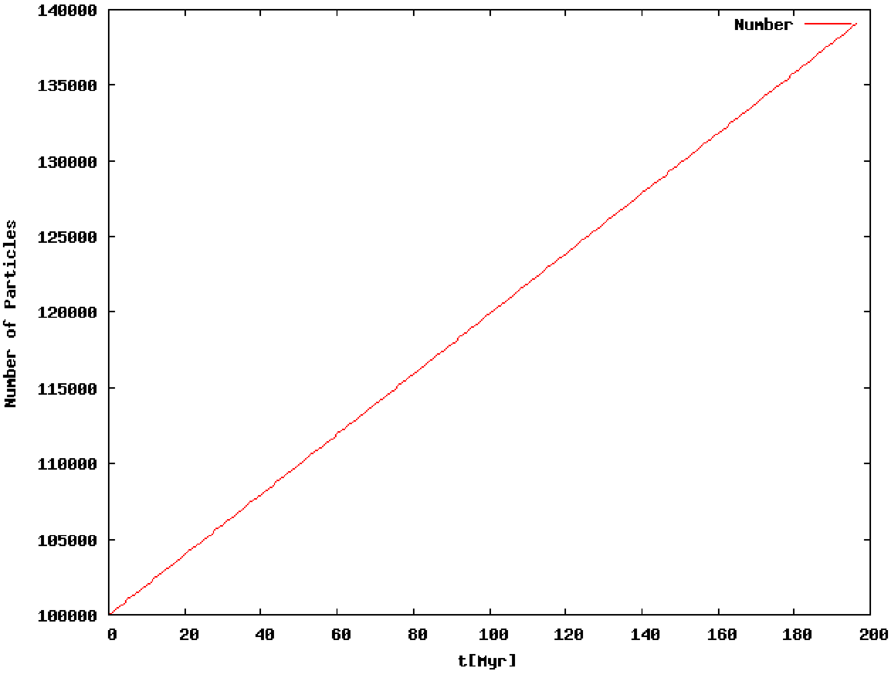

Fig. 3.13: Number of SPH-particles against time for the test simulation including gas accretion.

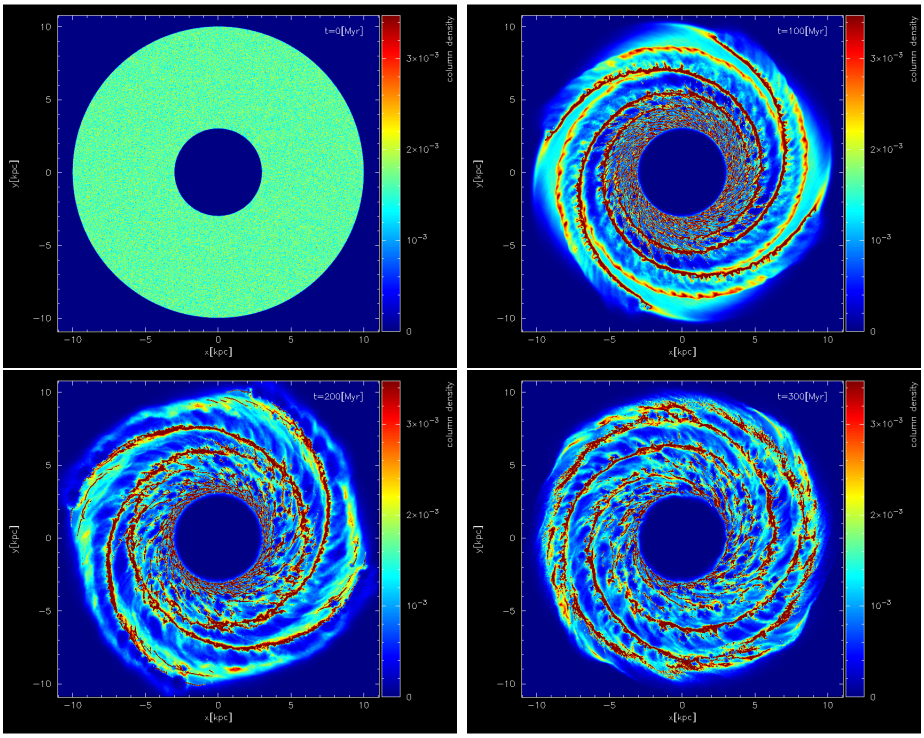

Fig. 3.14: Column density for the high resolution setup run after (upper left) $0Myr$, (upper right) $100Myr$, (lower left) $200Myr$, (lower right) $300Myr$.

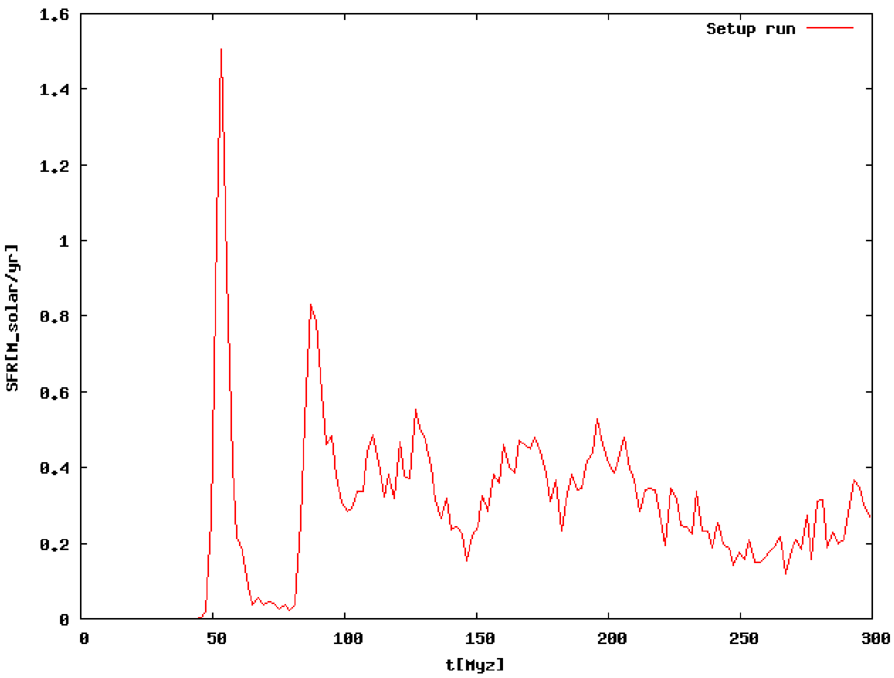

Fig. 3.15: Star formation rate versus time for the high resolution setup run.

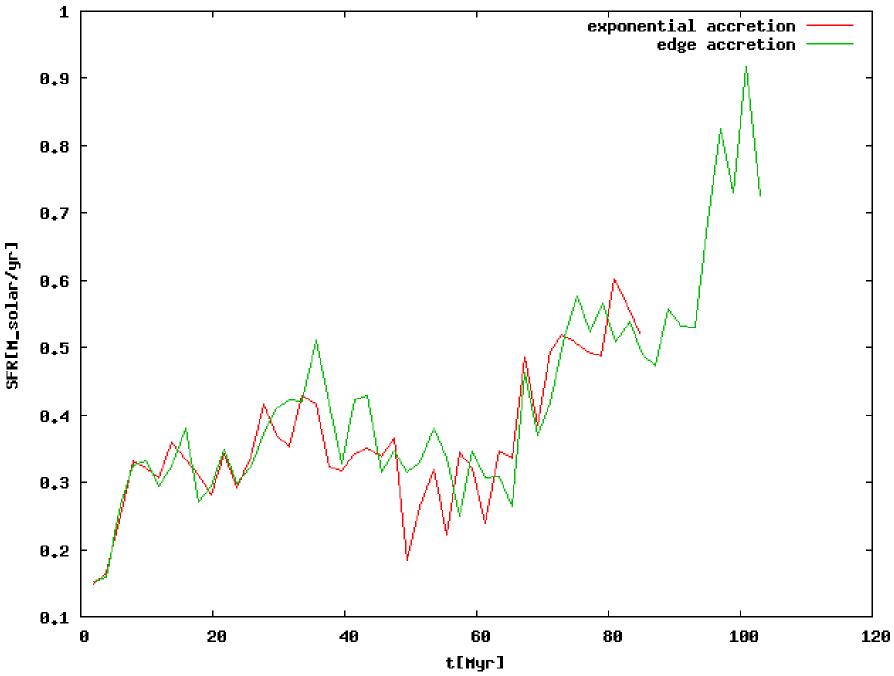

Fig. 3.16: Star formation rates for the runs with high accretion rate and (red) exponential radial distributions, or (green) injection at the edge of the disk.

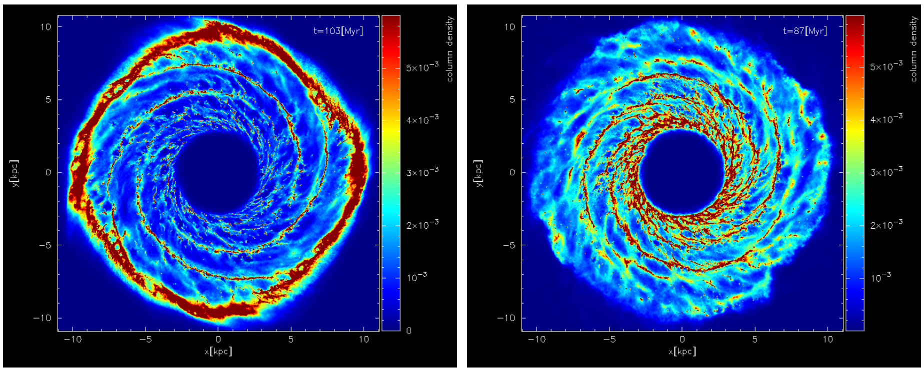

Fig. 3.17: Column densitis for the runs with injection at the edge of the disk (left), and injection with an exponential radial destribution (right).

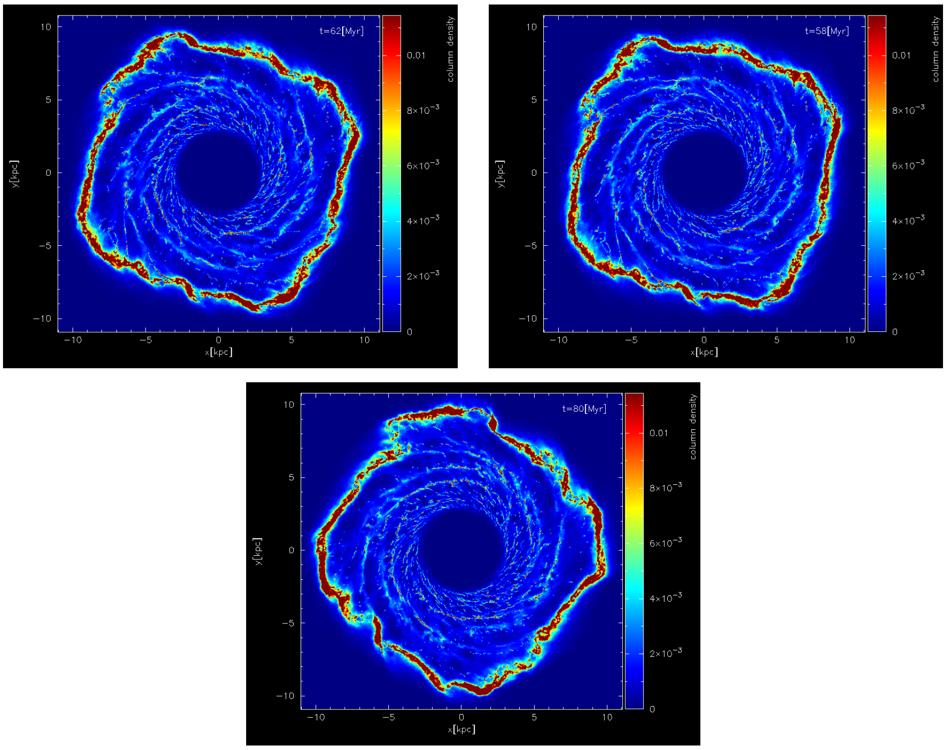

Fig. 3.18: Column densities for the simulations without any accretion(left), with accretion rate $0.8 M_{\odot}/yr$ (middle), and with accretion rate $1.6 M_{\odot}/yr$ (right).

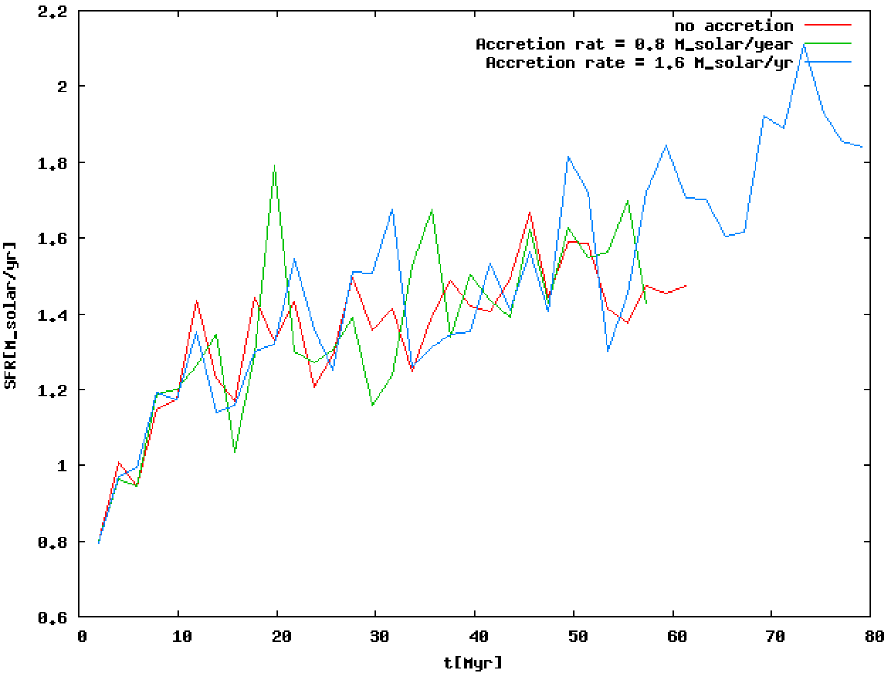

Fig. 3.19: Star formation rates for the simulations without accretion (red), with accretion rate $0.8 M_{\odot}/yr$ (green), and with accretion rate $1.6 M_{\odot}/yr$ (blue).

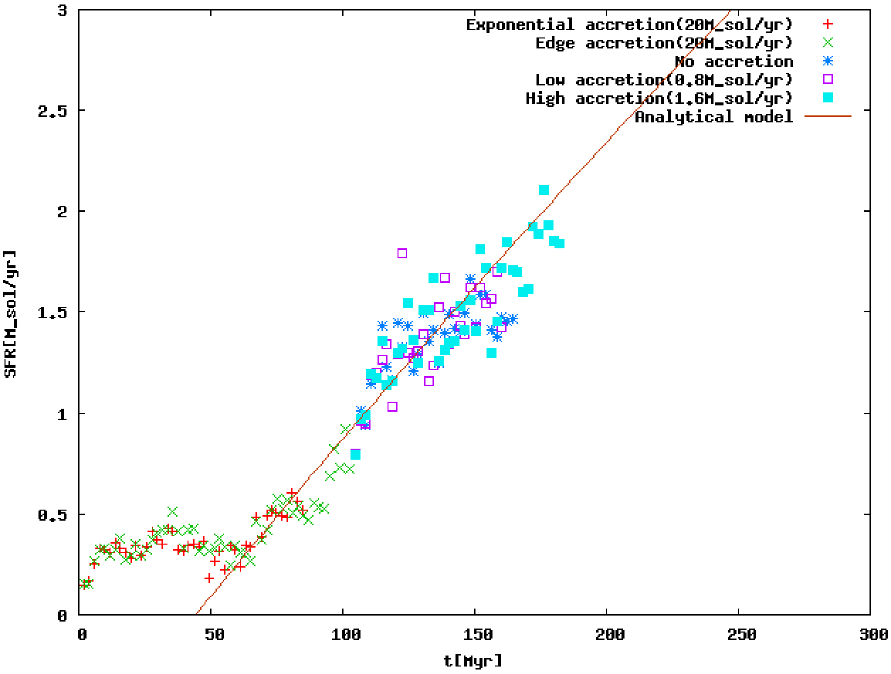

Fig. 3.20: SFRs for the simulations (coloured points) and the analytic model of equation 3.1 (solid line).

Summary and Conclusion

In this work we presented numerical implementations into the SPH-code GADGET3, that allows the study of the interaction between gas accretion and star formation. We have performed tests of a prescription for radiative processes in the interstellar medium that allow a two-phase medium to develop even in the absence of self-gravity. We introduced a self-consistent model of star formation and stellar feedback that further regulates the gas dynamics of a star forming system and takes into account the consumption of gas during star formation. Lastly we developed a routine that is capable of introducing new SPH-particles into an already running simulation in a numerically stable way. This routine is highly flexible and can easily be adapted to study many different accretion regimes, many more than we were able to present in this work. Our aim was to study a system that is self-regulated, where the star formation rate closely follows the accretion rate of cold gas, as one would expect from simple theoretical models. Our initial tests point in the right direction expected from theory, but unfortunately time limits forced us to expand this work to a scope that would allow an even more detailed treatment of the systems we were interested in. Furthermore, the high resolution run described in chapter 3.2.1 holds a wealth of information on the dynamics of a star forming gaseous disk that is only waiting to be closely investigated. In closing, we would like to point out once more that this work can be seen as preliminary work that opens up a new and interesting field of research that can now be studied with heretofore not possible detail. There is still a lot of work to be done until a satisfactory understanding of the link between star formation and accretion of cosmic gas is reached.

Aknowledgement

For all the help I received during the course of this work I'd like to thank

- Professor Andreas Burkert, for giving me the opportunity to work on this fascinating project, the many fruitful discussions, and for always showing great interest and giving support throughout the whole time.
- Christian Alig, for always knowing the answers to every problem that showed up, the great supervision, and generally being a treat to work with.
- Tadziu Hoffmann, for keeping the machines running against all odds, no matter what happened.
- Klaus Dolag, for having a vast pool of knowledge and expertise with the GADGET code, allowing him to give several very crucial hints at desperate times.
- All the members of the CAST group, for the generally nice work environment, doing very interesting research, and many conversations that taught me a lot about any topic imaginable.
- Christian Obermeier, Mihael Kodric, Florian Pils, Sabine Kretschmann, and all the other master students and PhD students, and people who work at the USM, for making the time spent there exceedingly enjoyable.
- My parents and family, for their overall support throughout my entire life and for having nurtured my interest in science from an early age, I wouldn't be where I am without them.
- Amy, for being awesome.
- My girlfriend Caterina, and all the others who stood by my side throughout the last year and gave me their support in difficult times.

Bibliography

E. L. O. Bakes and A. G. G. M. Tielens. The photoelectric heating mechanism for very small graphitic grains and polycyclic aromatic hydrocarbons. *The Astrophysical Journal*, 427:822–838, June 1994. doi: 10.1086/174188.

M. R. Bate and A. Burkert. Resolution requirements for smoothed particle hydrodynamics calculations with self-gravity. *Monthly Notices of the Royal Astronomical Society*, 288:1060–1072, July 1997.

V. Biffi, K. Dolag, and H. Böhringer. Investigating the velocity structure and X-ray observable properties of simulated galaxy clusters with PHOX. *Monthly Notices of the Royal Astronomical Society*, page 102, October 2012. doi: 10.1093/mnras/sts120.

J. Binney and S. Tremaine. *Galactic Dynamics.* Princeton University Press, 2008.

R. D. Blandford and J. P. Ostriker. Supernova shock acceleration of cosmic rays in the Galaxy. *The Astrophysical Journal*, 237:793–808, May 1980. doi: 10.1086/157926.

N. Bouché, A. Dekel, R. Genzel, S. Genel, G. Cresci, N. M. Förster Schreiber, K. L. Shapiro, R. I. Davies, and L. Tacconi. The Impact of Cold Gas Accretion Above a Mass Floor on Galaxy Scaling Relations. *The Astrophysical Journal*, 718:1001–1018, August 2010. doi: 10.1088/0004-637X/718/2/1001.

J. Brand, J. G. A. Wouterloot, and L. Magnani. Molecular gas and stars in the translucent cloud MBM 18 (LDN 1569). *Astronomy & Astrophysics*, 547:A85, November 2012. doi: 10.1051/0004-6361/201219822.

P. C. Clark, S. C. O. Glover, R. S. Klessen, and I. A. Bonnell. How long does it take to form a molecular cloud? *Monthly Notices of the Royal Astronomical Society*, 424:2599–2613, August 2012. doi: 10.1111/j.1365-2966.2012.21259.x.

D. P. Cox and G. C. Gómez. Analytical Expressions for Spiral Arm Gravitational Potential and Density. *Astrophysical Journal Supplement Series*, 142:261–267, October 2002. doi: 10.1086/341946.

A. Dekel, R. Sari, and D. Ceverino. Formation of Massive Galaxies at High Redshift: Cold Streams, Clumpy Disks, and Compact Spheroids. *The Astrophysical Journal*, 703:785–801, September 2009. doi: 10.1088/0004-637X/703/1/785.

C. Dobbs. Gas dynamics in whole galaxies: SPH. In J. Alves, B. G. Elmegreen, J. M. Girart, and V. Trimble, editors, *Computational Star Formation*, volume 270 of *IAU Symposium*, pages 459–466, April 2011. doi: 10.1017/S1743921311000810.

C. L. Dobbs, A. Burkert, and J. E. Pringle. Why are most molecular clouds not gravitationally bound? *Monthly Notices of the Royal Astronomical Society*, 413: 2935–2942, June 2011a. doi: 10.1111/j.1365-2966.2011.18371.x.

C. L. Dobbs, A. Burkert, and J. E. Pringle. The properties of the interstellar medium in disc galaxies with stellar feedback. *Monthly Notices of the Royal Astronomical Society*, 417:1318–1334, October 2011b. doi: 10.1111/j.1365-2966.2011.19346.x.

D. Espada, S. Komugi, E. Muller, K. Nakanishi, M. Saito, K. Tatematsu, S. Iguchi, T. Hasegawa, N. Mizuno, D. Iono, S. Matsushita, A. Trejo, E. Chapillon, S. Takahashi, Y. N. Su, A. Kawamura, E. Akiyama, M. Hiramatsu, H. Nagai, R. E. Miura, Y. Kurono, T. Sawada, A. E. Higuchi, K. Tachihara, K. Saigo, and T. Kamazaki. Giant Molecular Clouds and Star Formation in the Tidal Molecular Arm of NGC 4039. *ArXiv e-prints*, November 2012.

K. C. Freeman. On the Disks of Spiral and so Galaxies. *The Astrophysical Journal*, 160:811, June 1970. doi: 10.1086/150474.

S. Genel, A. Dekel, and M. Cacciato. On the effect of cosmological inflow on turbulence and instability in galactic discs. *Monthly Notices of the Royal Astronomical Society*, 425:788–800, September 2012. doi: 10.1111/j.1365-2966.2012.21652.x.

S. C. O. Glover and P. C. Clark. Star formation in metal-poor gas clouds. *Monthly Notices of the Royal Astronomical Society*, 426:377–388, October 2012. doi: 10.1111/j.1365-2966.2012.21737.x.

S. C. O. Glover and M.-M. Mac Low. Simulating the Formation of Molecular Clouds. I. Slow Formation by Gravitational Collapse from Static Initial Conditions. *Astrophysical Journal Supplement Series*, 169:239–268, April 2007. doi: 10.1086/512238.

S. Heß and V. Springel. Gas stripping and mixing in galaxy clusters: a numerical comparison study. *Monthly Notices of the Royal Astronomical Society*, 426:3112–3134, November 2012. doi: 10.1111/j.1365-2966.2012.21819.x.

M. Heyer, C. Krawczyk, J. Duval, and J. M. Jackson. Re-Examining Larson's Scaling Relationships in Galactic Molecular Clouds. *The Astrophysical Journal*, 699:1092–1103, July 2009. doi: 10.1088/0004-637X/699/2/1092.

D. Hollenbach and C. F. McKee. Molecule formation and infrared emission in fast interstellar shocks. III - Results for J shocks in molecular clouds. *The Astrophysical Journal*, 342:306–336, July 1989. doi: 10.1086/167595.

R. C. Kennicutt and N. J. Evans. Star Formation in the Milky Way and Nearby Galaxies. *Annual review of astronomy and ystrophysics*, 50:531–608, September 2012. doi: 10.1146/annurev-astro-081811-125610.

R. C. Kennicutt, Jr. Star Formation in Galaxies Along the Hubble Sequence. *Annual review of astronomy and ystrophysics*, 36:189–232, 1998. doi: 10.1146/annurev.astro.36.1.189.

M. Krumholz and A. Burkert. On the Dynamics and Evolution of Gravitational Instability-dominated Disks. *The Astrophysical Journal*, 724:895–907, December 2010. doi: 10.1088/0004-637X/724/2/895.

M. R. Krumholz and T. A. Thompson. The Relationship between Molecular Gas Tracers and Kennicutt-Schmidt Laws. *The Astrophysical Journal*, 669:289–298, November 2007. doi: 10.1086/521642.

M. R. Krumholz, C. D. Matzner, and C. F. McKee. The Global Evolution of Giant Molecular Clouds. I. Model Formulation and Quasi-Equilibrium Behavior. *The Astrophysical Journal*, 653:361–382, December 2006. doi: 10.1086/508679.

J.-M. Launay and E. Roueff. Fine-structure excitation of ground-state C/+/ ions by hydrogen atoms. *Journal of Physics B Atomic Molecular Physics*, 10:879–888, April 1977. doi: 10.1088/0022-3700/10/5/024.

D. McCammon and W. T. Sanders. The soft X-ray background and its origins. *Annual review of astronomy and ystrophysics*, 28:657–688, 1990. doi: 10.1146/annurev.aa.28.090190.003301.

C. F. McKee and J. P. Ostriker. A theory of the interstellar medium - Three components regulated by supernova explosions in an inhomogeneous substrate. *The Astrophysical Journal*, 218:148–169, November 1977. doi: 10.1086/155667.

S. J. Oliver, J. Bock, B. Altieri, A. Amblard, V. Arumugam, H. Aussel, T. Babbedge, A. Beelen, M. Béthermin, A. Blain, A. Boselli, C. Bridge, D. Brisbin, V. Buat, D. Burgarella, N. Castro-Rodríguez, A. Cava, P. Chanial, M. Cirasuolo, D. L. Clements, A. Conley, L. Conversi, A. Cooray, C. D. Dowell, E. N. Dubois, E. Dwek, S. Dye, S. Eales, D. Elbaz, D. Farrah, A. Feltre, P. Ferrero, N. Fiolet, M. Fox, A. Franceschini, W. Gear, E. Giovannoli, J. Glenn, Y. Gong, E. A. González Solares, M. Griffin, M. Halpern, M. Harwit, E. Hatziminaoglou, S. Heinis, P. Hurley, H. S. Hwang, A. Hyde, E. Ibar, O. Ilbert, K. Isaak, R. J. Ivison, G. Lagache, E. Le Floc'h, L. Levenson, B. L. Faro, N. Lu, S. Madden, B. Maffei, G. Magdis, G. Mainetti, L. Marchetti, G. Marsden, J. Marshall, A. M. J. Mortier, H. T. Nguyen, B. O'Halloran, A. Omont, M. J. Page, P. Panuzzo, A. Papageorgiou, H. Patel, C. P. Pearson, I. Pérez-Fournon, M. Pohlen, J. I. Rawlings, G. Raymond, D. Rigopoulou, L. Riguccini, D. Rizzo, G. Rodighiero, I. G. Roseboom, M. Rowan-Robinson, M. Sánchez Portal, B. Schulz, D. Scott, N. Seymour,

D. L. Shupe, A. J. Smith, J. A. Stevens, M. Symeonidis, M. Trichas, K. E. Tugwell, M. Vaccari, I. Valtchanov, J. D. Vieira, M. Viero, L. Vigroux, L. Wang, R. Ward, J. Wardlow, G. Wright, C. K. Xu, and M. Zemcov. The Herschel Multi-tiered Extragalactic Survey: HerMES. *Monthly Notices of the Royal Astronomical Society*, 424:1614–1635, August 2012. doi: 10.1111/j.1365-2966.2012.20912.x.

M. Schmidt. The Rate of Star Formation. *The Astrophysical Journal*, 129:243, March 1959. doi: 10.1086/146614.

F. H. Shu, R. J. Allen, S. Lizano, and D. Galli. Formation of OB Associations in Galaxies. *The Astrophysical Journal*, 662:L75–L77, June 2007. doi: 10.1086/519375.

L. Spitzer, Jr. The Dynamics of the Interstellar Medium. III. Galactic Distribution. *The Astrophysical Journal*, 95:329, May 1942. doi: 10.1086/144407.

V. Springel. The cosmological simulation code GADGET-2. *Monthly Notices of the Royal Astronomical Society*, 364:1105–1134, December 2005. doi: 10.1111/j.1365-2966.2005.09655.x.

V. Springel and L. Hernquist. A multi-phase model for simulations of galaxy formation. In J. Makino and P. Hut, editors, *Astrophysical Supercomputing using Particle Simulations*, volume 208 of *IAU Symposium*, page 273, 2003.

A. Toomre. On the gravitational stability of a disk of stars. *The Astrophysical Journal*, 139:1217–1238, May 1964. doi: 10.1086/147861.

R. B. Tully and J. R. Fisher. A new method of determining distances to galaxies. *Astronomy & Astrophysics*, 54:661–673, February 1977.

E. Vázquez-Semadeni, G. C. Gómez, A. K. Jappsen, J. Ballesteros-Paredes, R. F. González, and R. S. Klessen. Molecular Cloud Evolution. II. From Cloud Formation to the Early Stages of Star Formation in Decaying Conditions. *The Astrophysical Journal*, 657:870–883, March 2007. doi: 10.1086/510771.

M. G. Wolfire, D. Hollenbach, C. F. McKee, A. G. G. M. Tielens, and E. L. O. Bakes. The neutral atomic phases of the interstellar medium. *The Astrophysical Journal*, 443:152–168, April 1995. doi: 10.1086/175510.

B. Zuckerman and N. J. Evans, II. Models of massive molecular clouds. *The Astrophysical Journal*, 192:L149–L152, September 1974. doi: 10.1086/181613.

Selbstständigkeitserklärung

Hiermit versichere ich,

dass ich diese Masterarbeit zum Thema: "Selbstregulierte Sternentstehung in Galaktischen Scheiben, beeinflusst durch die Akkretion kosmischen Gases" selbstständig verfasst habe. Ich habe keine anderen als die angegebenen Quellen und Hilfsmittel benutzt, sowie Zitate kenntlich gemacht.
Mir ist bekannt, dass Zuwiderhandlung auch nachträglich zur Aberkennung des Abschlusses führen kann.

Ort, Datum

Unterschrift